Cement and Concrete Composites 149 (2024) 105511

Contents lists available at ScienceDirect

Cement and Concrete Composites

journal homepage: www.elsevier.com/locate/cemconcomp

Stability analysis of a granite-based geopolymer sealant for CO_2 geosequestration: In-situ permeability and mechanical behavior while exposed to brine

Seyed Hasan Hajiabadi [a,*], Mahmoud Khalifeh [a], Reinier van Noort [b]

[a] Department of Energy and Petroleum Engineering, Faculty of Science and Technology, University of Stavanger, 4036, Stavanger, Norway
[b] Department of Reservoir Technology, Institute for Energy Technology, Postbox 40, 2027, Kjeller, Norway

ARTICLE INFO

Keywords:
Geopolymer
CO_2 geosequestration
Brine exposure
In-situ permeability
Mechanical performance

ABSTRACT

When considering the use of geopolymers (GPs), as potential alternatives for Portland cement, high durability during exposure to brine at encountered downhole is a key requirement. This study delves into the response of a granite-based GP system designed especially for CO_2-geosequestration upon exposure to brines with different concentrations of NaCl. Exposure was carried out by imposed flow in a triaxial apparatus, at 90 °C and 13.8 MPa confining pressure. Mechanical properties were tested in the same apparatus once exposure was completed. A suite of micro-scale analytical techniques was then used to assess the GP's microstructure, mineralogical composition, and chemical bonding. The obtained results revealed increasing compressive strength with increasing brine salinity, suggesting greater resistance to deformation and potential cracking. Concurrently, decreasing Poisson's ratios and increasing Young's moduli could lead to an elevated risk of mechanical failure under strain. In addition, following a 3-week injection period, permeability of NaCl-flooded samples decreased by 20%–35% from initial values. Analysis of the effluents showed fluctuations in the pH and ion content with time, mainly attributed to complex chemical interactions including cation exchange, silicate dissolution and hydrolysis, precipitation of alkali-enriched gels, and mineral alterations. Micro-scale analyses revealed that the improved durability is linked with the formation of new minerals, especially zeolites in the presence of NaCl or portlandite when deionized water was introduced. In conclusion, this study presents new data on the durability of a rock-based GP system when exposed to brine and elevated pressure and temperature, offering insights for optimization to downhole environments.

1. Introduction

Carbon Capture and Storage (CCS) in geological formations is a crucial strategy for mitigating climate change, as acknowledged by the Intergovernmental Panel on Climate Change (IPCC) [1–3]. Saline aquifers, owing to their substantial storage capacities and broad geographical distribution, as well as depleted oil and gas reservoirs, due to the proven effectiveness of their caprocks and the existence of suitable injection infrastructure, are the most viable geological formations for long-term CO_2 sequestration [4–6]. However, in particular in reservoirs containing high-salinity brine, this brine can trigger geochemical reactions with Ordinary Portland Cement (OPC), the predominant material used for wellbore isolation, potentially leading to increased permeability and subsequent CO_2 leakage [7–9]. Sealant integrity may be further complicated by local stresses and salt crystallization-induced stress-strain alterations of mechanical behavior [10–15]. These integrity issues have been highlighted in both laboratory research and field-scale observations [16–19].

Geopolymers (GPs) offer a promising alternative to OPC, and have recently gained significant attention [20–22]. GPs are low Ca-content alkali-activated materials that can be synthesized by activating reactive precursors with varying aluminosilicate contents using alkali-based activators such as (combinations of) NaOH, KOH, Na_2SiO_3, and K_2SiO_3 [23–26]. Key benefits of well-designed GPs over OPC include high acid resistance, rapid strength development, and low chemical shrinkage, making such GPs primary candidates for cementing the wellbores in CCS operations and hydrocarbon reservoirs [27–32].

Recent literature highlights the potential of rock-based materials,

* Corresponding author.
E-mail address: Seyed.h.hajiabadi@uis.no (S.H. Hajiabadi).

https://doi.org/10.1016/j.cemconcomp.2024.105511
Received 31 December 2023; Received in revised form 29 February 2024; Accepted 8 March 2024
Available online 11 March 2024

particularly granite, as precursors for GPs [24,28,33–36]. Despite crystalline phases, these materials are classified as GPs due to their aluminosilicate composition, cohesive structure formed, and mineralogical transformations during geopolymerization [37]. Furthermore, the inclusion of slag and micro-silica ensures the presence of crucial amorphous components. Reactive slags act as early strength enhancers, accelerating the geopolymerization rate by promoting the formation of calcium aluminosilicate hydrate (C-A-S-H) gels [25,38–40]. Research indicates that the coexistence of sodium/potassium aluminosilicate hydrate (N,K)-A-S-H and C-A-S-H gels in GPs enhances internal confinement and compressive strength, and lowers the permeability of the system [21,41–47]. Additionally, micro-silica serves as a reactive micro-filler, adjusting the SiO_2/Al_2O_3 ratio, facilitating the formation of nucleation sites necessary for geopolymerization, and further reducing the GP's permeability [48–51]. However, excessive micro-silica can induce self-desiccation and cracking, necessitating careful control of its amount for optimal performance [21,49].

The current body of literature investigating the impact of brine exposure on GP systems at elevated pressures and temperatures encountered in downhole conditions shows a strong dependence on both GP composition, and exposure conditions, highlighting the need for further research to close existing knowledge gaps [21,30,32,41,52–54]. The conventional static-exposure technique, frequently employed to replicate downhole conditions, is constrained by inherent limitations arising from the establishment of equilibrium conditions, leading to notable experimental artefacts. Such limitations are commonly addressed through a renewal approach, for example by replacing the brine solution at set intervals during autoclave aging. Nevertheless, this method has its own drawbacks, including thermal shocks and depressurization-pressurization cycles induced during each fluid renewal, potentially causing substantial structural damage to the materials tested [19]. In addition, in batch/autoclave conditions, fluid penetration into the samples tested is mostly limited to diffusive transport. These limitations can be overcome by using imposed-flow exposure, in which a flow of fluid is driven through the exposed sample by a pressure gradient, leading to deeper fluid penetration within a reduced timeframe.

In addition, the existing literature on GP systems cured in brine solutions is limited in scope, particularly in terms of comprehensive micro-scale analysis. This limitation often results in inconsistent findings, with certain investigations noting diminished performance of GPs under brine exposure [30,32,44], while others suggest augmented mechanical durability [41,52,55]. The absence of thorough effluent analysis further exacerbates this situation, preventing the conclusive demonstration of underlying causes for these discrepancies, thereby promoting hypothesized explanations, such as reduced alkali leaching [30,32,41,44,52,55]. Further details on previous findings regarding the impact of brine exposure on GPs or OPC, as well as their response to chlorine attack or hydrothermal conditions, can be found in Table A1 in the Appendix.

In this work, we assess the impact of brine exposure on the mechanical behavior and permeability of a granite-based GP system specifically developed for CO_2 geosequestration. An imposed-flow technique is employed, injecting NaCl brines with a range of salinity levels (0–15 wt%) through cured cylindrical GP samples. After exposure, a comprehensive range of micro-scale analytical techniques is employed to investigate the link between the GP system's mechanical attributes and its mineralogy, morphology, and chemical bonding, and thus gain further insights into the factors impacting the system's stability.

2. Materials and methods

2.1. Materials

A low Ca-content GP system (containing less than 10 wt% CaO) was developed by combining a naturally occurring aluminosilicate rock as the primary precursor with active quenched Ground Granulated Blast Furnace Slag (GGBFS) and a small amount of commercially obtained micro-silica, mainly consisting of ultra-fine amorphous SiO_2 spheres. The aluminosilicate rock used in the experiment was a powdered granite sourced as a quarrying byproduct from southwestern Norway, with particle sizes ranging from 5 to 150 μm, to which no additional modifications were made.

Tables 1 and 2 present the chemical composition and physical properties, respectively, of the constituents comprising the solid phase of the prepared GPs.

The activating hardener employed was a potassium silicate solution with a modulus ratio (SiO_2/K_2O) of 2.14. Deionized water (DW) was added to regulate the water content and viscosity of the system, and to serve as a solution medium for the chemicals. The workability of the mixed system was tuned using an in-house-developed retarder based on zinc nitrate hexahydrate ($Zn(NO_3)_2.6H_2O$) and potassium nitrate (KNO_3) (0.64 wt%).

2.2. Preparation of the GP system

The granite-based GP system used in this study was prepared according to the procedures described in Hajiabadi, Khalifeh and van Noort [37]. Precise proportions of the constituent raw materials employed in the formulation of the GP system are presented in Table 3. The content of retarders and the K^+/Zn^{2+}-ratio were determined based on the results of several laboratory experiments conducted and reported previously [37,56,57]. To ensure system homogeneity, the solid phase was added to the liquid phase after a 24-h rest period, and the mixing process was conducted using a Waring high-speed blender equipped with an OFITE control pad, in accordance with the procedures recommended by API RP 10B-2 [58].

2.3. Samples conditioning and curing

After the mixing process, the GP slurries were conditioned at 60 °C, using an atmospheric consistometer, gradually raising the temperature from room temperature at a rate of 1 °C/min. Subsequently, the slurries were subjected to stirring at 150 rpm and 60 °C for a duration of 30 min. The purpose of this procedure was to replicate the conditions to which the slurries would be exposed during downhole placement. Additionally, the conditioning process ensured slurry homogeneity and minimized thermal shock to the specimens upon the subsequent static curing conditions in autoclaves [37]. These autoclaves were maintained at a constant temperature of 90 °C, as the selected bottomhole static temperature (BHST), and were connected to high-precision pumps to sustain a curing pressure of 13.8 MPa, as the selected bottomhole static pressure (BHSP). Once the samples had been cured at these conditions for one week, the autoclaves were cooled down and then depressurized gradually, taking care to avoid rapid changes in temperature and pressure that might impact GP integrity [58].

2.4. Tri-axial experiments

To evaluate the impact of brine-exposure on the mechanical behavior of the GP, tri-axial tests were conducted on samples prepared as described above. The experiments followed the recommended procedures outlined in API TR 10TR7 2017 [59]. The ends of the specimens were ground flat and parallel on a lathe to ensure uniform distribution of axial stresses applied throughout the tests. During the tri-axial tests, an extensometer was positioned around the middle of each specimen to continuously monitor radial deformation, while the axial displacement was measured using a Linear Variable Differential Transformer (LVDT) connected to the top of the loading piston.

Each tri-axial test consisted of three distinct stages: the hydrostatic stage, waterflooding, and the deviatoric stage. To start a test, the sample was heated to 90 °C at a controlled rate of 1 °C/min. After a one-night rest period to ensure thermal stability, a hydrostatic load of 13.8 MPa

Table 1
Chemical composition of the constituents within the solid precursor used in this work, based on XRF analyses.

Elements[a] (wt.%)	Si	Al	Fe	Mg	Ca	Na	K	Ti	P	S	Mn
Granite	32	7.3	2.5	0.6	1.4	2.2	5.1	0.3	0.1	<0.1	<0.1
GGBFS	16	6	0.2	7	25	0.4	0.8	1.8	<0.1	1.2	0.4
Micro-silica	46	<0.1	<0.1	0.1	0.1	<0.1	0.5	<0.1	<0.1	0.1	<0.1

[a] The elements are calculated as oxides and normalized to 100%, but reported as elements (wt.%).

Table 2
Physical properties of the constituents within the solid precursor used in this work.

Physical properties[a]	d_{10} (μm)	d_{50} (μm)	d_{90} (μm)	Density (g/cm^3)	Specific surface area (m^2/kg)
Granite	3.52	21.1	131	2.63	631
GGBFS	2.79	15.9	46.6	2.90	944
Micro-silica	0.19	0.34	0.6	2.29	19320

[a] d_{10}, d_{50}, d_{90} represent the percentiles of particle-size distribution. Specific surface area was measured through BET analysis.

was applied by simultaneously applying axial and radial stresses at a constant loading rate of 5 MPa/min. Once the desired pressure and temperature conditions were reached, the sample was allowed to equilibrate for another 3–4 h. After that, a flow of brine containing set concentrations of NaCl (0, 5, 10, and 15 wt%) was forced through the GP sample for three weeks, set at a constant flow rate. During this time, the upstream pressure was continuously recorded, while the downstream pressure was kept atmospheric. By continuously monitoring the differential pressures across the samples at set injection rates, sample permeabilities could be tracked in real time based on Darcy's law [60,61]. Samples of the effluent fluid were collected at specific intervals, for chemical analysis. Note that as the permeabilities of the samples decreased, injection pressures at set flowrate increased. For some samples, as the injection pressures approached the limiting value set roughly 10% below the confining pressure at 12.5 MPa, the imposed flowrate needed to be reduced. Imposed flowrates are plotted against time in Fig. 1a. For one sample, GP-BR-5NaCl, due to its low initial permeability, the flowrate had to be reduced multiple times, and a steady flow was not achieved for most of the exposure duration. It should also be noted that when the maximum pressure on the injection pump was triggered, this lead to a break in the fluid injection until the pump could be reset.

Subsequent to the waterflooding period, axial loading was increased at a constant loading rate of 10 MPa/min and through a consolidated-drained (CD) deviatoric regime. The loading rates employed in the tests were in accordance with the recommended values outlined in API TR 10TR7 2017, which range from 3.5 to 14 MPa/min [59]. One reference sample was also subjected to identical conditions over the same duration, but without exposure to a flow of DW or brine.

Table 4 presents the experimental parameters for each GP sample, including exposure time, exposure fluid, and NaCl concentration in the exposure fluid. Note that prior to the exposure tests, all GP samples underwent a one-week curing regime within an autoclave set at 90 °C and 13.8 MPa.

2.5. Sample characterization

After triaxial exposure and testing, the induced alterations in sample composition and microstructure were assessed using a range of analyses techniques. The chemical bonds present within the GP systems were assessed using Fourier transform infrared spectroscopy (FTIR) utilizing an Agilent Carry 630 instrument. The mineral composition of the samples was determined using X-ray diffraction (XRD) analysis performed on a Bruker-AXS Micro-diffractometer D8 Advance. The XRD analysis employed a Cu-Kα radiation source with a wavelength (λ) of 1.5406 Å, operating at 40 kV and 25 mA, and diffraction patterns were recorded over a 2θ range of 5–70°. Furthermore, the microstructures of the cured and exposed materials were examined using a Zeiss Supra 35VP scanning electron microscope (SEM) equipped with a backscattered electron detector (BSD) and an energy dispersive spectroscopy (EDS) analyzer. Brunauer-Emmett-Teller (BET) surface areas of exposed GP samples were determined using a TriStar II 3020 instrument with N_2, in order to assess the effects of mineralogical alterations on the accessible surface area, and thereby, the pore structure of GP samples.

To prepare the samples for these analyses, they were initially dried at 40 °C overnight and subsequently stored in a vacuum-dryer for one day to eliminate any remaining moisture. SEM-EDS studies were carried out on fractured sections, while parts of the samples were powdered for XRD, FTIR, and BET analyses. Prior to BET analyses, powdered samples were sieved, to attain a particle size <63 μm, improving homogeneity and minimizing particle size impact on the measured surface areas, and subsequently vacuum-sealed and degassed at 100 °C for an hour.

Additionally, the pH of fluid samples taken during the flooding experiments was measured at room temperature, using a digital pH meter (Orion Research, model 201). Fluid sample chemical compositions were analyzed on an Agilent 5800 ICP-OES and Thermo Scientific Element XR HR-ICP-MS, on samples that were filtered through 0.45μ filters and diluted with 2% suprapur nitric acid to proper concentrations of targeted elements.

3. Results and discussion

3.1. In-situ permeability measurements

Based on the set flowrates and measured injection pressures, sample permeabilities could be monitored continuously, once a steady state flow had been achieved. Fig. 1b plots in-situ permeability against time for all samples. Note that permeabilities can only be assessed once flow has become steady (after changing the flowrate); as such steady flow was only achieved briefly in GP-BR-5NaCl, permeability curves are not available for most of that exposure.

It should also be noted that while all GP samples originated from the

Table 3
A list of mix design parameters of the GP slurry used in this work.

Components	Solid phase			Liquid phase				
	Granite	GGBFS	Micro-silica	DW	K-silicate solution	NaOH pellets	$Zn(NO_3)_2.6H_2O$	$K(NO_3)$
Mass (gr)	490	200	10	57	314	0.5	5.28	1.65

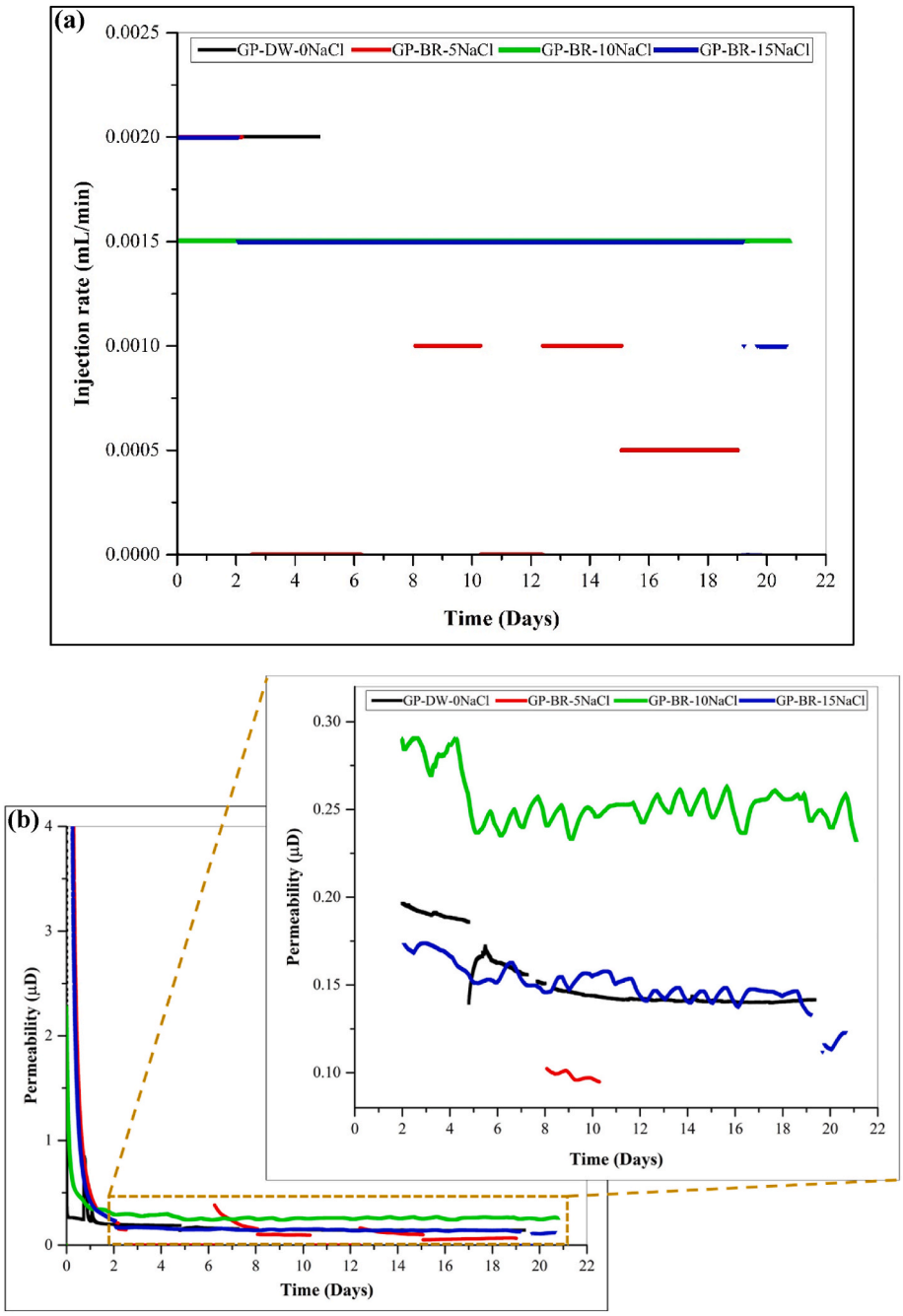

Fig. 1. An illustration of the alterations of (a) injection rates and (b) GPs' permeability throughout the injection period. GP-DW-0NaCl represents exposure to distilled water, while GP-BR-5NaCl, GP-BR-10NaCl, and GP-BR-15NaCl were exposed to brines containing 5%, 10%, and 15% NaCl, respectively.

Table 4
Experimental parameters and exposure conditions for the GP samples employed in this work.

Sample ID	Curing time	Exposure time	Exposure fluid	NaCl concentration (wt.%)
RGP (Reference)	1 week	3 weeks	–	–
GP-DW-0NaCl	1 week	3 weeks	DW	0
GP-BR-5NaCl	1 week	3 weeks	Brine	5
GP-BR-10NaCl	1 week	3 weeks	Brine	10
GP-BR-15NaCl	1 week	3 weeks	Brine	15

same mix design, the observed variations in initial permeability stem from the inherent heterogeneity of geopolymeric materials, primarily influenced by complex geopolymerization reactions. These variations are very small, considering that the permeability unit is μD, and they fall within an acceptable range.

Table 5 presents the changes in in-situ permeability of GP samples under simulated downhole conditions throughout a three-week exposure to brines with varying NaCl concentrations. As shown, the permeabilities of all GP samples decreased during the 3-week injection periods. However, a consistent trend between sample permeability and

Table 5
The permeability alterations of GP samples throughout three-week exposure period at simulated downhole conditions.

Sample No.	Permeability (μD)		Permeability reduction (%)
	Initial[a]	Final	
RGP (Reference)	–	–	–
GP-DW-0NaCl	0.196	0.141	28
GP-BR-5NaCl	0.100	0.065	35
GP-BR-10NaCl	0.290	0.233	19.7
GP-BR-15NaCl	0.173	0.123	28.9

[a] Measured upon reaching steady conditions (48 h after the initiation of DW/brine injection).

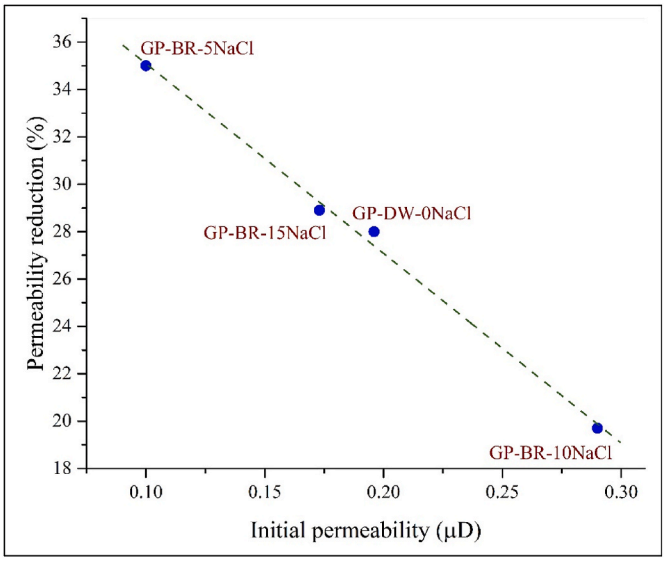

Fig. 2. Permeability reduction in the GP samples flooded with different NaCl concentrations plotted against their initial permability values.

brine salinity was not readily apparent. Note, however, that all samples permeabilities are more than an order of magnitude lower than the minimum values required by (for example) NORSOK D010 (<5μD) [62].

Fig. 2 demonstrates a linear relationship between permeability alterations and the initial permeability of GP specimens, irrespective of the NaCl concentration in the brine. Specifically, lower-permeability GP samples display an increased susceptibility to more pronounced permeability reductions. This can be due to the reduced size of pore throats in lower-permeability specimens, which makes them more prone to clogging or plugging.

3.2. In-situ mechanical properties

To assess the mechanical performance of the GP samples, their compressive strengths, Young's moduli, and Poisson's ratios were determined as critical parameters indicating the material's resistance to

Table 6
Compressive strength, Young's modulus, and Poisson's ratio of the GP samples according to Tri-axial test analyses.

Sample ID	Compressive strength (MPa)	Young's modulus (GPa)	Poisson's ratio
RGP (Reference)	45.63	3.98	0.33
GP-DW-0NaCl	41.17	4.92	0.24
GP-BR-5NaCl	56.20	6.96	0.27
GP-BR-10NaCl	52.06	6.04	0.17
GP-BR-15NaCl	59.76	6.54	0.20

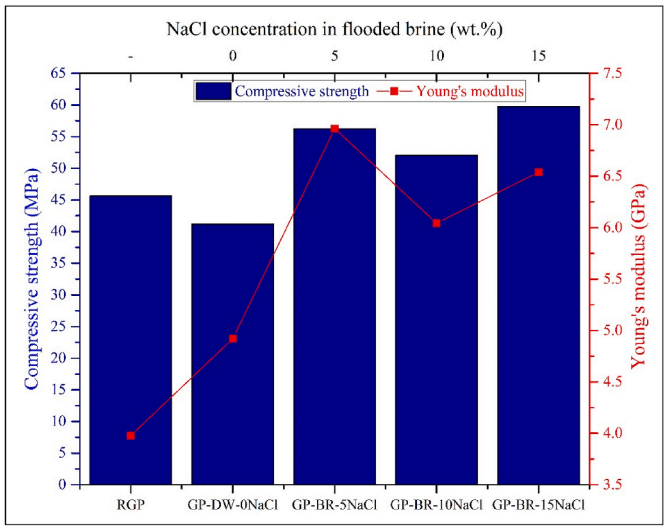

Fig. 3. The in-situ compressive strength and Young's modulus of the GP samples flooded with brines of different NaCl concentrations at simulated downhole conditions of 90 °C and 13.8 MPa.

deformation and overall stiffness (See Table 6 and Fig. 3). Compared to the reference sample (RGP) that was aged without imposed fluid flow, brine-exposed samples have considerably higher compressive strengths. The compressive strength of the sample flooded with DW (GP-DW-0NaCl) was significantly lower than that of RGP.

Additionally, GP samples flooded with brines (GP-BR-5NaCl, GP-BR-10NaCl, and GP-BR-15NaCl) demonstrated higher Young's moduli compared to both the reference (RGP) sample and the DW-flooded (GP-DW-0NaCl) sample. As a higher Young's modulus means that the material is less able to accommodate deformation elastically, this indicates that exposure to higher salinity levels may result in a greater risk of cracking under fixed strain. It is worth noting that the flexibility of cementitious materials is commonly linked to their strength development: as strength increases, flexibility decreases [31,61].

In addition, the results also indicate a decrease in Poisson's ratio of the GP system with higher brine salinities. This implies a higher risk of destructive hoop stresses and potential mechanical failure [63]. The stiffening effect of NaCl on the GP system thus also reduces the system's ability to deform laterally, leading to increased localized stresses upon strain, making the material more vulnerable to strain.

3.3. Sample characterization

3.3.1. XRD analysis

Fig. 4 presents the XRD analysis results for all GP samples after exposure. Note that phase identification utilized DIFFRAC.EVA software, while phase quantification was not performed. The software estimated crystallinity content by comparing the assigned areas of amorphous content, indicated by characteristic humps in the XRD patterns, with the crystal peaks. This comparative analysis yielded relative values rather than precise measurements. For detailed sample XRD patterns, refer to Fig. A1 in the Appendix.

Estimated crystalline contents (see Table 7) show that exposure to brines with higher NaCl contents leads to increased crystalline content in the GP system. In GP systems, such higher crystalline contents are commonly associated with enhanced network connectivity, mechanical strength, and Young's modulus [64–68]. For more detailed information, the individual XRD patterns of each GP sample are provided in the Appendix.

Further inspection of the XRD analyses shows that all GP samples exhibited similar mineral distributions. However, samples GP-BR-10NaCl and GP-BR-15NaCl displayed more prominent peaks for quartz

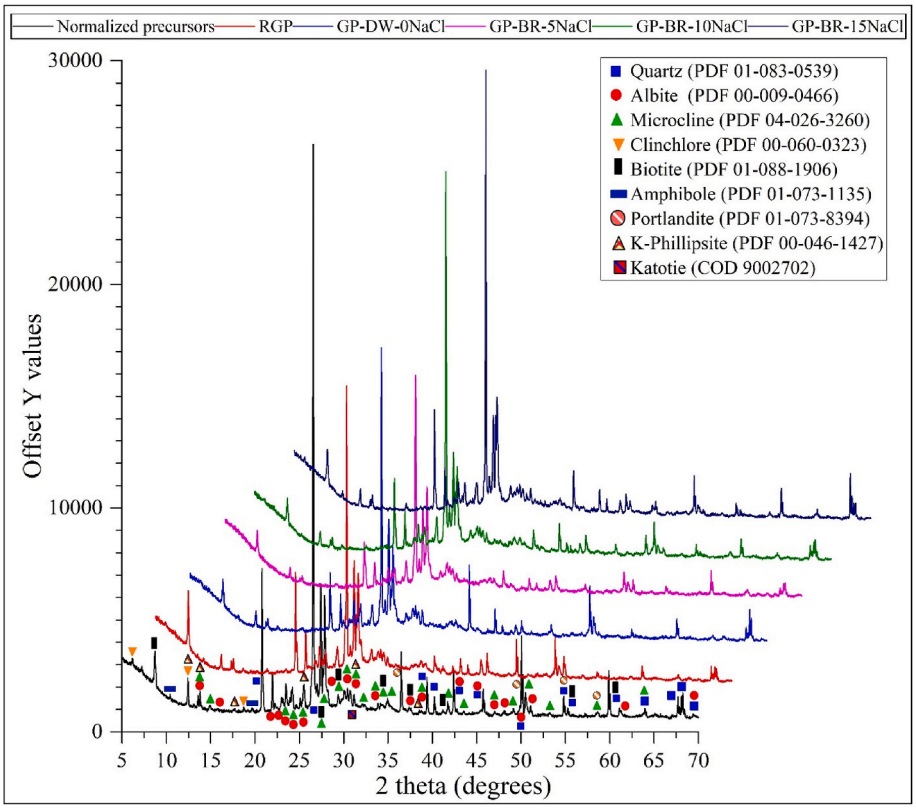

Fig. 4. XRD analysis of the normalized precursors, and RGP, GP-DW-0NaCl, GP-BR-5NaCl, GP-BR-10NaCl, and GP-BR-15NaCl after three-week exposure period at simulated downhole conditions.

Table 7
The crystalline content of the GP samples observed through XRD analysis.

Sample ID	Crystallinity (%)
RGP (Reference)	59.6
GP-DW-0NaCl	60.9
GP-BR-5NaCl	61.7
GP-BR-10NaCl	62.3
GP-BR-15NaCl	64.8

and feldspars (albite and microcline) and relatively less prominent peaks for chlorite, biotite, and amphibole. These differences, together with the 3–5% increase in crystalline content, point to accelerated reaction rates in GP systems exposed to NaCl-based brines, leading to the consumption of minerals that had not yet dissolved, such as micas and amphiboles, and the subsequent formation of more stable minerals through condensation and polymerization processes [69–71]. Higher NaCl concentrations resulted in increased intensities of peaks associated with zeolites (K-Phillipsite) and the emergence of hydrogarnet (kotoite) in the XRD patterns. These secondary minerals are likely formed due to significant ion exchange triggered by elevated NaCl levels, and contributed to the higher crystalline content in the GP system. In contrast, the GP sample flooded with DW (GP-DW-0NaCl) exhibited a higher quantity of portlandite ($Ca(OH)_2$) and lower K-Phillipsite content compared to NaCl-exposed samples.

Moreover, comparing the mineralogical content of GP samples, GP-BR-5NaCl and GP-BR-15NaCl exhibited an increase in the relative quantity of albite compared to microcline. These observations are consistent with previous findings, indicating that the increased intensity of the albite peak signifies a higher degree of polymerization, contributing to improved compressive strength in the samples [68].

3.3.2. FTIR analysis

FTIR analysis was performed on all GP samples to assess the impact of fluid injection on the types of chemical bonds present in the GP samples. The results are presented in Fig. 5. The absorption peaks at 965-978 cm^{-1} are caused by asymmetric stretching vibrations of Si–O-T (T = Si, Al, K). Additional peaks at 715-721 cm^{-1} correspond to symmetrical stretching vibrations of Si–O–Si and Si–O–Al bonds, while peaks related to hydroxyl group stretching ((Si, H)–O–H bonds) appears at 3328-3399 cm^{-1}. The bending vibrations of hydroxyl groups (H–O–H) at 1634-1638 cm^{-1} are attributed to absorbed or imprisoned water in cavities [72–74]. The bands at 1408-1463 cm^{-1} indicate O–C–O bond stretching, characteristic of carbonate groups. They also indicate the presence of calcium/sodium carbonates resulting from GP sample carbonation [74–77].

The results show a shift towards higher wave numbers (and thus shorter bond lengths) in the Si–O-T asymmetric stretching peaks in GP-BR-10NaCl and GP-BR-15NaCl (to 972 cm^{-1} and 978 cm^{-1}, respectively) compared to the unexposed and DW-flooded samples (RGP at 967 cm-1, and GP-DW-0NaCl, at 965 cm^{-1}). This shift towards shorter bonds can be explained by formation of new crystalline phases, formation of more robust (C,N,K)-A-S-H gels, and implies significant polycondensation and the promotion of network connectivity within the GP matrix [73–75,78]. The reduced –OH band intensity also signifies increased polycondensation and the maturation of GPs. On the other hand, enhanced –OH bands, especially in GP-DW-0NaCl, result from increased hydrolysis of the silicate gel surfaces, correlating to its coarsened porous structure, and to its reduced mechanical strength [73,75].

3.3.3. BET surface area analysis

BET analyses were performed on powdered samples of the exposed GP systems (<63 μm). The obtained results provide insight into the impact of exposure on the surface characteristics of the GP system, and

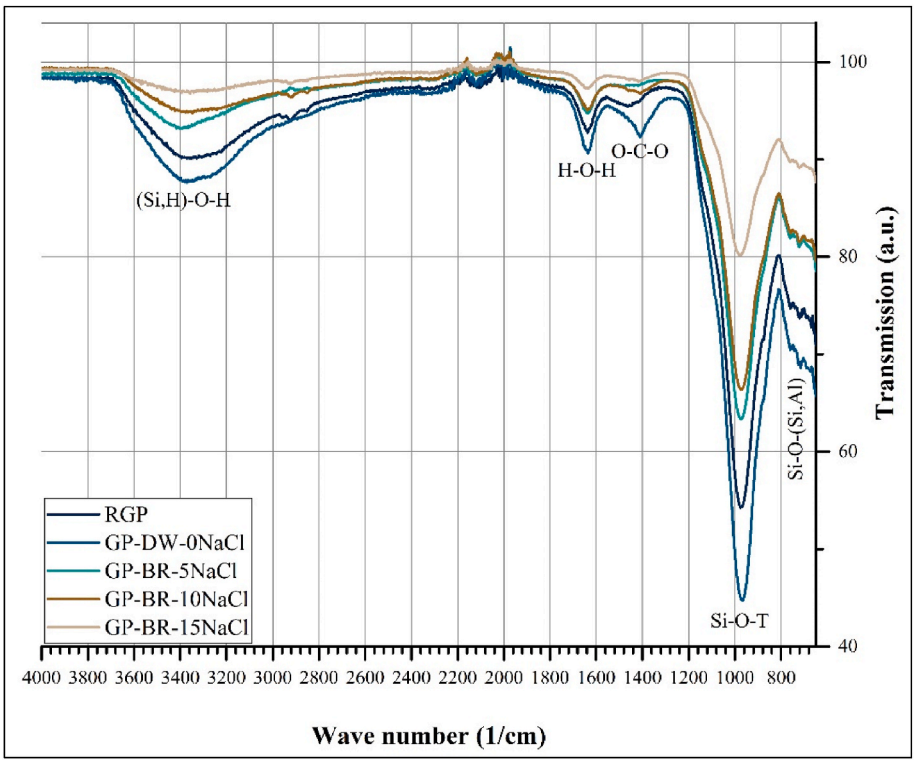

Fig. 5. Fourier Transform Infrared Spectroscopy (FTIR) spectrum of the unexposed and exposed GP samples to brines of different NaCl concentrations at simulated downhole conditions of 90 °C and 13.8 MPa.

Table 8
The BET surface area of the GP samples after three-week exposure period at simulated downhole conditions.

Sample ID	S_{BET} (m^2/g)
RGP (Reference)	44.41
GP-DW-0NaCl	23.52
GP-BR-5NaCl	31.43
GP-BR-10NaCl	104.41
GP-BR-15NaCl	108.41

offer further quantitative insight into the changes in porosity and crystallinity.

As shown in Table 8, sample GP-DW-0NaCl (exposed to DW) had an approximately 47% lower specific surface area than the reference sample (RGP). Similarly, sample GP-BR-5NaCl (5 wt% NaCl) showed a 29% decrease in specific surface area compared to RGP. A decrease in the specific surface area of a GP can be attributed to enhanced dissolution, primarily driven by the continual hydrolysis of silicate species exposed to deionized or low-salinity water. This prolonged hydrolysis results in a reduction in adsorption surface area.

Conversely, the samples exposed to brines containing 10 wt% and 15 wt% NaCl showed increases in specific surface area of 135% and 144%, respectively, compared to the reference sample. This increase in specific surface area could be related to changes in the pore network associated with the formation of new crystalline phases, as zeolites have high specific surface areas due to their crystal structures [66,79,80].

3.3.4. *Microstructural analysis using SEM*

Fractured GP specimens were studied using an SEM-BSD with EDS

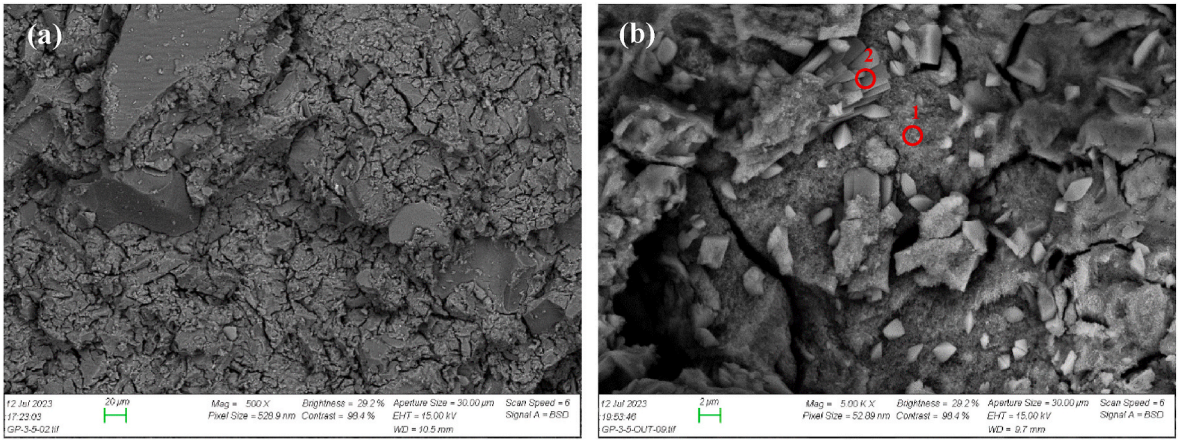

Fig. 6. SEM images of RGP (unflooded sample) after three-week curing at simulated downhole conditions of 90 °C and 13.8 MPa. Points (1) and (2) depict the elemental ratios and morphological traits associated with (C, K)-A-S-H gels and zeolites, respectively.

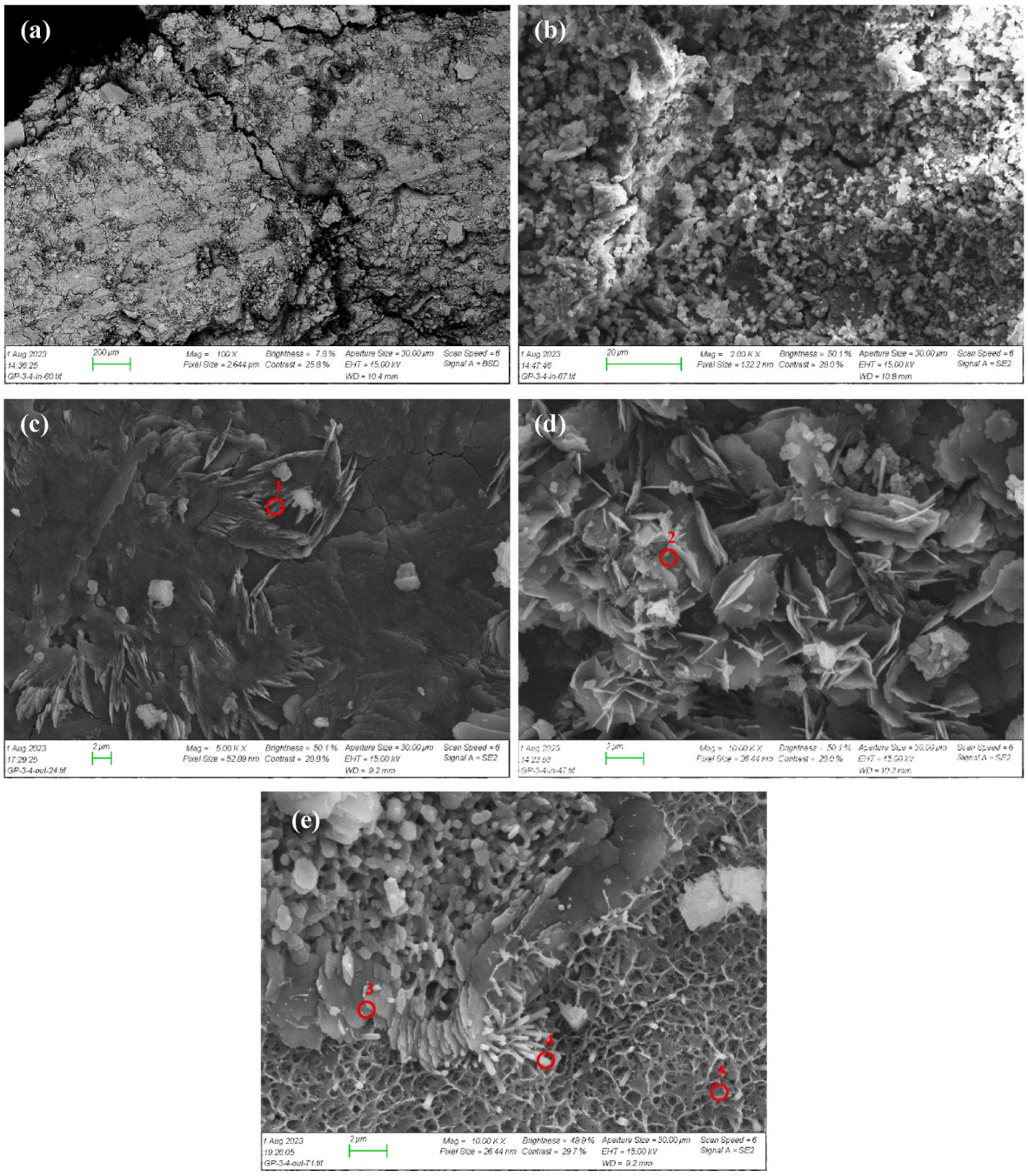

Fig. 7. SEM images of GP-DW-0NaCl flooded with DW at simulated downhole conditions of 90 °C and 13.8 MPa. Points 1, 2, and 3 represent portlandite, while Point 4 depicts the elemental ratios and morphological characteristics suggestive of zeolites (likely K-Phillipsite). Point 5 corresponds to (C, K)-A-S-H gels with their honeycomb structure.

analyses. While the polished samples are recommended for SEM-EDS analysis, the fractured samples were intentionally used in these experiments to prevent from compromising the morphology of the samples. Selected micrographs, along with their EDS analyses are presented in Figs. 6–10. Noteworthy is that the mineral identification stems from the analysis of elemental ratios (e.g., Si/Al, Si/O, Si/Ca, etc.) coupled with micrograph observations from the SEM images. By scrutinizing the elemental content of each point and comparing it with the suspected phases, as well as correlating it with the observed micrograph morphology, the phases were recognized.

SEM-BSD/EDS analysis of the RGP(unflooded) sample (Fig. 6) reveals the persistence of unreacted precursor particles within the GP matrix. EDS analysis of the matrix further confirms the presence of (C, K)-A-S-H gels, characterized by their typical honeycomb structures, occupying intergranular pore spaces within the GP framework [81]. These gels act as a binding agent, filling the voids between larger particles, thereby enhancing material strength, while their amorphous nature contributes to ductility. Additionally, a limited observation of micron-sized grains is noted, displaying elemental ratios and grain morphology suggestive of potential zeolite presence (see Fig. 6b). Note that the matrix shows numerous fine cracks, which were most likely the result of drying shrinkage induced during sample preparation within the vacuum chamber, and were not present during the experiments.

SEM-micrographs taken on sample GP-DW-0NaCl (exposed to DW) are shown in Fig. 7. Fig. 7a and b, highlight the marked presence of dissolved zones (black zones in Fig. 7a) alongside unreacted particles,

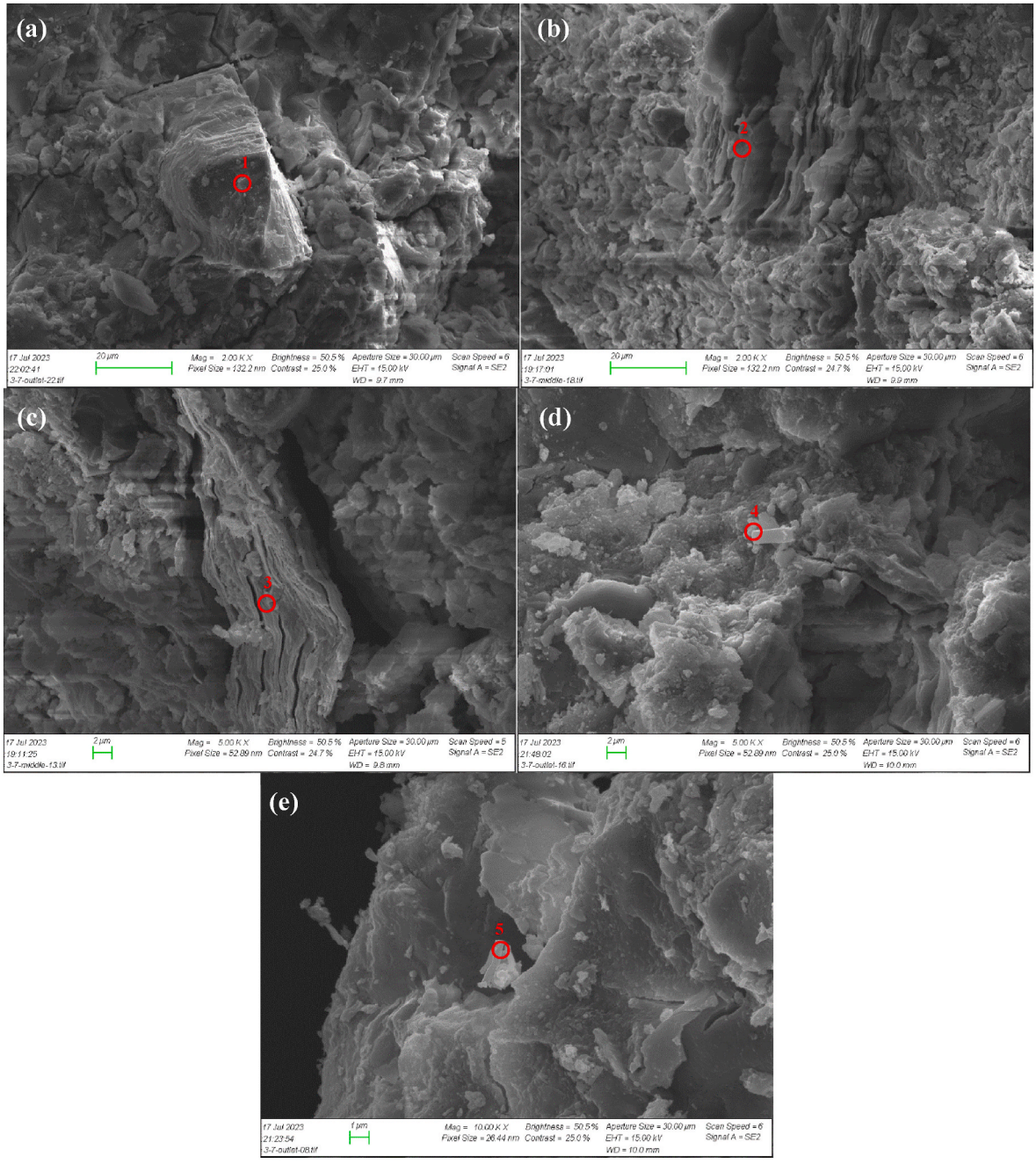

Fig. 8. SEM images of GP-BR-5NaCl flooded with brines of 5 wt% NaCl concentration at simulated downhole conditions of 90 °C and 13.8 MPa. Points 1, 2, and 3 correspond to quartz, clinochlore (chlorite), and biotite, respectively. Points 4 and 5 depict the elemental ratios and morphological characteristics of zeolites, presumably K-Phillipsite.

both embedded within an amorphous matrix, composed of gel, that is less compact than the gel observed in reference sample RGP. Furthermore, the gel matrix is seen to consist largely of loosely embedded particles of <1 to ~2 μm in size (Fig. 7b). The dissolution of matrix can be attributed to the increased breakage of Si–O–Si bonds due to the hydrolysis of silicate species, and reduced polycondensation/recrystallization processes in the absence of NaCl. Furthermore, Fig. 7c, d, and 7e clearly depict the presence of considerable quantities of plate-like portlandite ($Ca(OH)_2$) and a limited occurrence of newly formed grains of K–Ca–Al-silicates. These grains, exhibiting characteristic composition and grain morphology resemblances to zeolites, likely K-Phillipsite, are surrounded by (C, K)-A-S-H gels. These observations highlight the reduced contribution of Ca^{2+} to the reactions in the absence of NaCl, which leads to the precipitation of these ions as $Ca(OH)_2$ within the GP system and formation of less compact structures.

Considering the SEM observations on samples exposed to NaCl-containing brines, we see that such exposure induced notable microstructural changes, particularly evident at higher NaCl concentrations. SEM-EDS analysis of sample GP-BR-5NaCl (5 wt% NaCl) demonstrated the enhanced dissolution of precursor minerals such as quartz, chlorite, and biotite in the presence of NaCl, resulting in the increased precipitation of (C, K)-A-S-H gels, thus creating a more robust geopolymeric network. Limited formation of zeolites, likely K-Phillipsite, was also observed within the GP matrix (Fig. 8d–e).

After exposure to 10 wt% NaCl brine, unreacted minerals still persist within the GP system (such as the feldspar grains easily recognized from

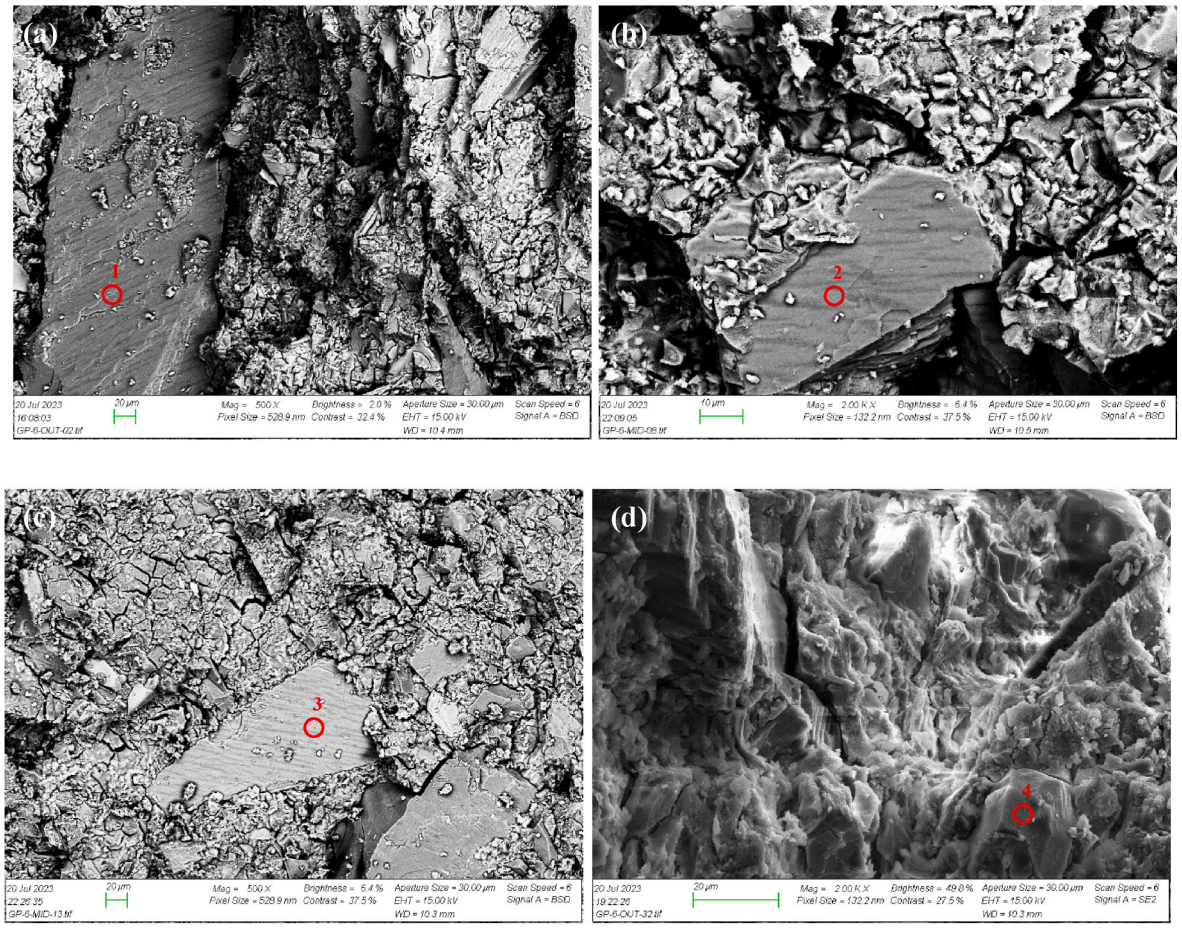

Fig. 9. SEM images of GP-BR-10NaCl flooded with brines of 10 wt% NaCl concentration at simulated downhole conditions of 90 °C and 13.8 MPa. Points 1, 2, and 3 represent microcline, while Point 4 depicts the composition and morphological characteristics of hydrogarnet (Katoite).

their exsolution lamellae depicted in Fig. 9a, b, and 9c). Additionally, an increased abundance of new minerals, resembling hydrogarnets (Katoites) in grain shape and composition, is observed within the GP matrix (see Fig. 9d). The formation of these minerals might be due the enhanced reactivity of the $Ca(OH)_2$-aluminosilicate-water system in the presence of NaCl, as discussed in literature [82,83]. Furthermore, both precursor grains and newly formed minerals are tightly enclosed by a geopolymeric gel binder.

After exposure to 15 wt% NaCl brine, substantial quantities of zeolite (most likely K-Phillipsite) are observed covering the microstructure of the GP-BR-15NaCl sample. This substantive zeolite formation implies a catalytic impact of elevated concentrations of NaCl on the mineralogical composition of the GP. As shown in Fig. 10e, zeolite nucleation and precipitation takes place at the honeycomb nodes of the (C, K)-A-S-H gel. Under favorable conditions, this process leads to a complete transformation of (C, K)-A-S-H gels into zeolite, with the (C, K)-A-S-H gels within the GP systems as a transitional phase towards that conversion [84]. These zeolitic minerals, in turn, may be a transitional phase as well, as they may further react to form more stable aluminosilicate minerals such as feldspathoids and feldspars [84,85]. Note that on the SEM micrographs presented in Fig. 10f, the appearance of thin crusts of NaCl are identified based on EDS. However, these most likely formed as a result of pore fluid evaporation during sample handling and storage between testing and SEM imaging.

3.3.5. *Characterization of the effluents*

Fig. 11a illustrates the changes in effluent pH against time, observed throughout the three-week flooding experiments. When interpreting the results, it is imperative to account for the subtle impact of interconnected porosity, a parameter not directly measured in this study. Depending on this parameter, the time required for one pore volume of fluid to traverse the sample could range from approximately 1 day (assuming a very low accessible porosity of 2%) to about 9 days (assuming a porosity of about 20%). This range, consequently, leads to the transit of 2.5–20 pore volumes of fluid throughout each individual test.

The results show that during injection of DW and low-salinity (5 wt% NaCl) brine, effluent pH decreased nearly continuously, from initial values of 13.7 to 13.0. However, injecting brines containing NaCl concentrations of 10 wt% and 15 wt% resulted in an initial increase in effluent pH from 11.8 to 13.0, to a peak of 12.8 and 13.4 after 9 days, followed by a continuous decrease down to 11.2 and 11.7.

When considering the Si-concentrations in the effluent samples (see Fig. 11b), higher concentrations are measured in the DW and 5 wt % NaCl samples than in the samples from experiments with higher NaCl-contents. Furthermore, the Si ion concentrations for these latter effluents show similar trends with time as observed in the pH-measurements, increasing initially, and then decreasing.

In Fig. 11c–a notable observation emerges: notably lower effluent Na concentrations compared to the injected brine. Furthermore, while Na-concentrations in the effluent of the samples flooded with DW and low-salinity brine are nearly constant, or decrease slowly, in the GP samples exposed to higher NaCl concentrations, pronounced increases in effluent Na-concentration occur over the injection period, commencing approximately at 0.4 and 0.5 normalized injection time for the GP-BR-10NaCl and GP-BR-15NaCl effluents, respectively. It should be noted that the injection rates for the GP-BR-5NaCl sample were lower due to the specimen's lower initial permeability.

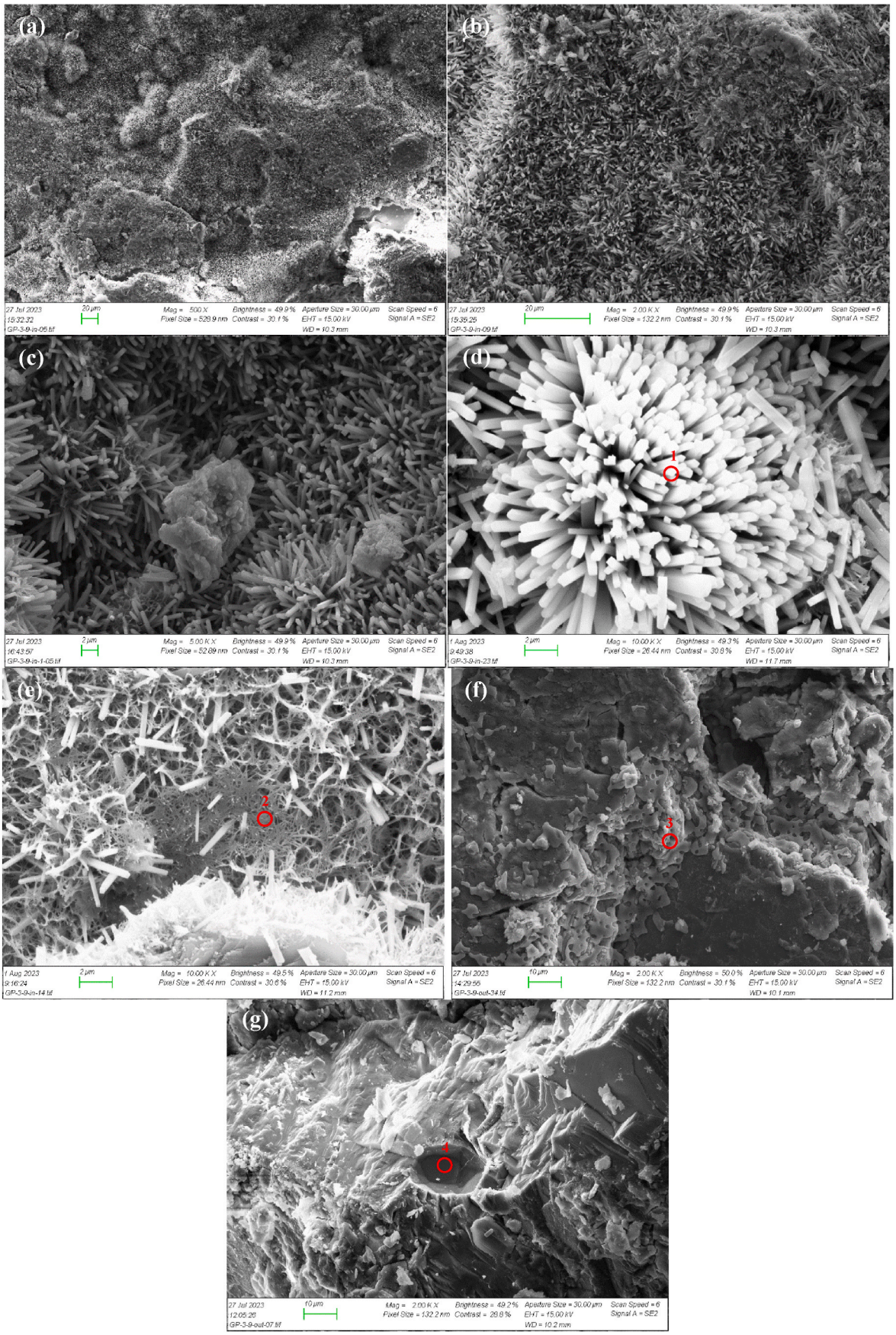

Fig. 10. SEM images of GP-BR-15NaCl flooded with brines of 15 wt% NaCl concentration at simulated downhole conditions of 90 °C and 13.8 MPa. Points 1, 2, and 3 represent Zeolite (K-Phillipsite), (C, K)-A-S-H, and NaCl, respectively, while Point 4 corresponds to Hydrogarnet (Katoite).

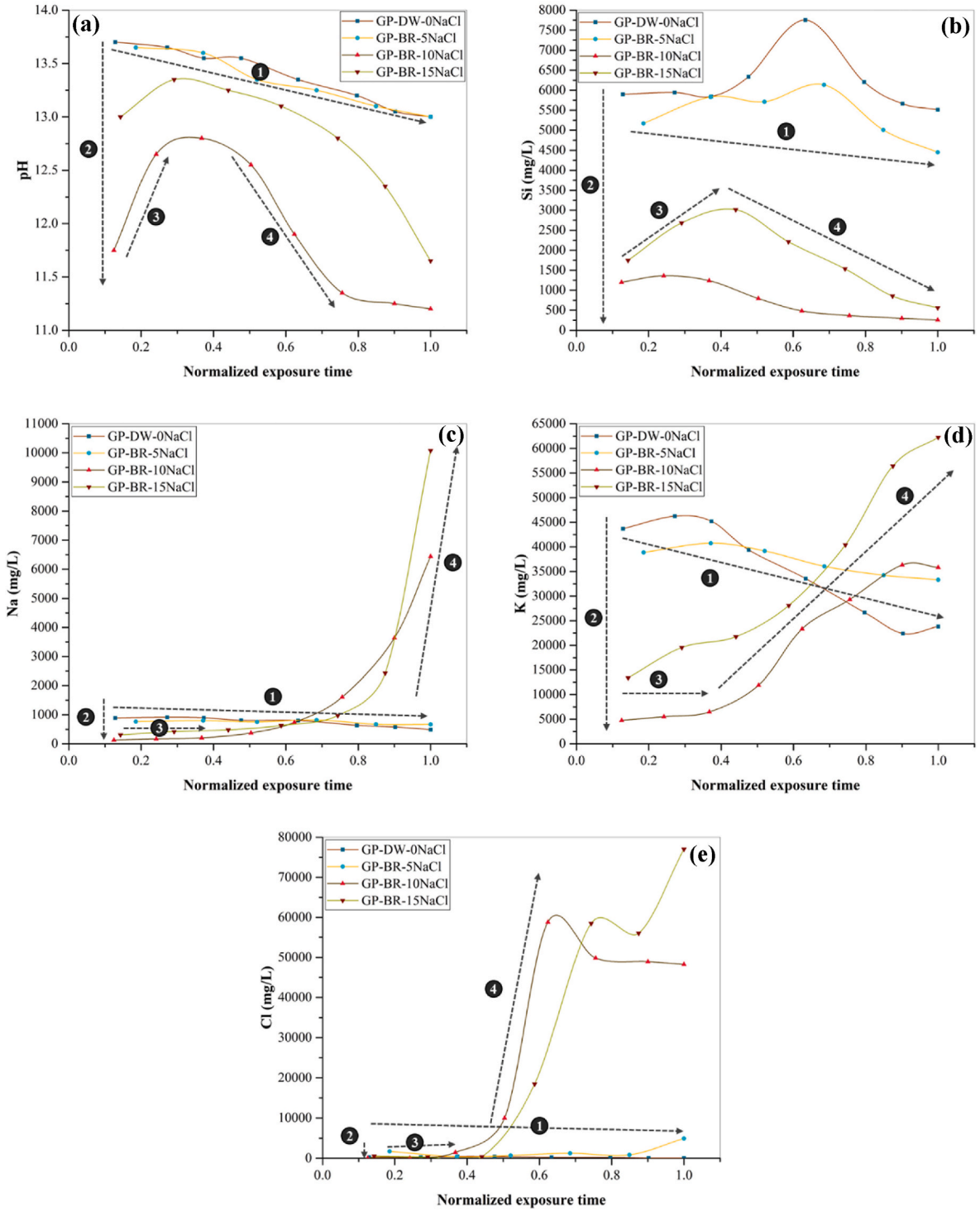

Fig. 11. An illustration of alterations in (a) pH, (b) Si ion content, (c) Na ion content, (d) K ion content, and (e) Cl ion content in the effluent of the GP samples throughout the normalized exposure time.

Furthermore, in Fig. 11d, presenting the K-ion content in effluent samples, GP-DW-0NaCl and GP-BR-5NaCl effluents show high initial K-contents. However, in the sample exposed to 0 wt% brine, this concentration initiates a decline after approximately 0.4 normalized exposure time, persisting continuously until the end of the experiment. Similarly, in the sample exposed to 5 wt% brine, the K-ion content in the effluent begins to decrease after 0.5 normalized exposure time. In contrast, K-ion contents are initially considerably lower in the effluents from GP-BR-10NaCl and GP-BR-15NaCl, followed by an increase after approximately 0.4 and 0.5 normalized exposure time, respectively.

Fig. 11e, finally, shows Cl-measurements performed using HR-ICP-MS. Initial Cl levels across all samples are notably low. For the DW-exposed sample, effluent Cl concentrations remain consistently low throughout the testing period. Conversely, in all samples exposed to NaCl, although initial Cl concentrations are also low, they exhibit an increasing trend over time. Specifically, in the case of 5 wt% NaCl exposure, there is a modest increase in effluent Cl content observed in the final sample, occurring after 0.85 to 1 normalized exposure time. In

the 10 wt% NaCl exposure, Cl concentrations begin to rise in the third effluent sample, taken between 0.25 and 0.36 normalized exposure time, peaking rapidly before stabilizing at a slightly lower level for the remainder of the experiment. In the 15 wt% NaCl exposure, effluent Cl content shows a rapid increase in the fourth effluent sample, taken between 0.44 and 0.58 normalized exposure time, continuing to rise with some variability until the end of the experiment.

The interpretation of the observed trends in effluent composition is intricately tied to the assumed interconnected pore volume. If the accessible interconnected pore volume is low, it implies that the entire pore network would have undergone flushing before the initial fluid sample was collected. Conversely, assuming a higher brine-accessible interconnected pore volume necessitates consideration of the extended time required for displacing the first pore volume in the interpretation of the results.

3.3.5.1. Low accessible interconnected pores. Under the assumption of low brine-accessible interconnected pore volume, the interconnected pore network was completely flushed before the collection of the first effluent sample. Consequently, the observed trends in pH and ion concentrations can be explained as follows:

Path 1: During injection of DW or low-salinity brine, first, high-pH pore solution fluid is displaced from the sample, after which dissolution of KOH from the GP leads to the high observed effluent pH. The subsequent decrease in pH as exposure continues can then be ascribed to a depletion of KOH from the GP samples, as well as the dissolution of silica from K-silicate and other silicates, and the dissociation of dissolved H_4SiO_4 (This also contributes the bump in Si-contents observed in these samples after some exposure time) [86–89]. During further injection, as KOH and reactive (K-)silica become more depleted, effluent pH and K- and Si-contents decrease. In addition, for GP-BR-5NaCl, the Na-content in the effluents is much lower than the injected Na-concentration, indicating that Na is taken up by the sample. This could be through cation exchange mechanisms, where Na adsorbs on mineral surfaces, releasing cations trapped there (e.g., K), but Na may also be bound in new phases being precipitated (such as (C,N,K)-A-S-H gels).

Path 2: The lower initial pH of effluent pH of the samples flooded with higher-salinity brines compared to that of DW- and low-salinity brine is ascribed to the counterbalancing of pH-increasing reactions by the cation exchange reactions where Na^+ adsorbs on silica surfaces, causing the release of H^+ ions from those surfaces. Na^+ ions initiate the formation of $Si-O^-$ bonds within the framework of the GP structure, followed by the formation of H_2O and $Si-O^-Na^+$. This process reduces the initial pH and Na-ion content of pore solution in the samples flooded with higher-salinity brines compared to DW and low-salinity brine flooded samples (Eq. (1)):

$$\equiv Si-OH+Na^+ + OH^- \rightarrow \equiv Si-O^- + Na^+ + H^+ + OH^- \rightarrow \equiv Si - O^-Na^+ + H_2O \quad (1)$$

At the same time, the competition between Na^+ and pre-existing K^+ ions in the GP system is crucial. In the presence of a substantial amount of K^+ ions, as in the GP system employed in this study, the generated $\equiv Si-O^-$ bonds (from the reaction described above) undergo stochastic occupation through competitive interactions between Na^+ and K^+ ions [89]. Eq. (2) describes the reaction that might occur between K^+ ions and $\equiv Si-O^-$ triggered by Na^+:

$$\equiv Si-O^- + K^+ + H^+ + OH^- \rightarrow \equiv Si-O^-K^+ + H_2O \quad (2)$$

Reactions described in Eqs. (1) and (2) contribute to the significant reductions in the Na^+ and K^+ ion contents, respectively, observed in the effluent of samples exposed to higher NaCl concentrations compared to the sample exposed to DW and low salinity brine. Moreover, the decreased pH of the injected fluid at higher NaCl concentrations, in comparison to the samples exposed to DW and low-concentration brine, leads to a reduced rate of silica dissolution, thus a declined Si ion content in the injected fluid.

Path 3: Competing mechanisms and reactions contribute to the initial increasing trend observed in pH and Si ion content in the pore solutions of high-salinity brine-flooded samples. The previously mentioned diminishing pH trend, attributed to Na- and K-adsorptions on silica surfaces consuming OH^-, slows down as the surfaces become partially saturated with Na and K. Simultaneously, another mechanism increases OH^- content, where continued NaCl ingress elevates NaOH concentration within the GP's pore solution. This process, facilitated by reactions with $Ca(OH)_2$, significantly contributes to the initial pH increase [88]:

$$Ca(OH)_2 + 2NaCl \leftrightharpoons Ca(Cl)_2 + 2NaOH \quad (3)$$

This corresponds to increased Cl content in effluents from samples exposed to higher NaCl concentrations, which coincide with elevated K levels, indicating K^+ ion release from the sample to balance Cl^- ions. It is worth noting that Ca content in these effluents was below detectable limits, implying that Ca remains within the pore network. In addition, literature suggests that solutions containing alkali-group cations enhance the dissolution of quartz and amorphous silica, with evidence of a 30-fold increase in amorphous SiO_2 dissolution rates observed in NaCl-containing solutions; however, Li^+ and K^+ have been demonstrated to have similar impacts on silica dissolution rates [87,89]. As the released silica diffuses away from the surface and into the flowing pore fluid, this contributes to the initial rise in Si ion content in the effluent of the high salinity-flooded GP samples [82,83]. Simultaneously, $\equiv Si-O^-$ bonds, formed through the hydrolysis of silanol groups, contribute to the adsorption of Na^+ and K^+ ions. This adsorption contributes to the observed consistent trends of Na^+ and K^+ ions.

The interactions involving diffused silica ions, Na^+, and K^+ ions in the presence of water may result in the development of alkali-rich N(K)-A-S-H gels [88]. However, in the presence of NaCl, when free $Ca(OH)_2$ is available, ion-exchange processes can lead to the partial transformation of N(K)-A-S-H gels into Ca-rich gels enveloping the reactive particles (Eq. (4)) [82,83,88]:

$$N(K)-A-S-H + Ca(OH)_2 \leftrightharpoons (C,N,K)-A-S-H \quad (4)$$

The effects of this reaction are visible in the SEM micrograph in Fig. 8a, where a dissolving quartz grain is seen that is surrounded by (C,K)-A-S-H gels. Once such (C,N,K)-A-S-H gels have formed, the introduced (Na,K)-enriched medium can initiate a sequence of ion exchange mechanisms within these gels, leading to the formation of secondary minerals. Specifically, these ion exchange processes can facilitate the development of stable and well-organized nanocrystals within the gels (see Fig. 10e). These nanocrystals subsequently serve as nuclei for polymerization and rearrangement of the gels, and lead to the transformation of the gels into zeolites [80,83,90,91].

Path 4: A sharp increase in the effluent Na-content indicates that the ability of the sample to take up Na+ from the injected fluid is becoming saturated. K-contents continue to increase as well, as dissolution of K continues, while the ability of the sample to take up K in new phases is saturated (by Na^+). Simultaneously, there is also decrease in pH and Si-content, suggesting that the reactions releasing OH- are taking place at lower rates, and (potentially as a result of the lower pH) Si-release reactions are also slowing down.

It should be noted that the lower Na ion content in effluents compared to the injected fluid indicates Na^+ adsorption in the system. In addition, under elevated NaCl concentrations, effluent K-ion contents exceed Na-contents. The observed phenomenon is ascribed to the smaller size and increased mobility of Na^+ ions relative to K^+. This discrepancy leads to the initiation of ion exchange within K-bearing components, potentially inducing mineralogical modifications similar to the albitization of K-rich alkali feldspars [92,93].

3.3.5.2. High accessible interconnected pores. Considering a scenario

where a larger interconnected pore volume is assumed for GP samples, implying incomplete flushing of the pore network before the initial sample collection, the data can be interpreted within the framework of a displacement mechanism that is not fully miscible.

In samples exposed to brine, the movement of injected fluid in the porous network is discernible due to the significantly higher concentrations of Na and Cl ions in the injected fluid compared to the pore fluid. This detection relies on monitoring points where concentrations of these elements in the effluents show notable increases. In the case of the GP-BR-5NaCl sample, Cl appears in the effluent between 0.85 and 1 normalized exposure time, corresponding to an injected brine volume of approximately 19.2–22.6 mL. Interestingly, there is no observable increase in Na concentration in the effluent during this test. For the GP-BR-10NaCl and GP-BR-15NaCl specimens, initial increases in Cl content are observed between 0.25 and 0.36 (10 wt% NaCl – minor increase) and 0.44 to 0.58 (15 wt% NaCl – strong increase) normalized exposure time, equivalent to an injected brine volume of about 16–21 mL. Notably, correlating these Cl content increases to effluent Na content reveals a delayed onset of Na content increase. Furthermore, Na contents remain relatively low compared to Cl contents, suggesting Na uptake in the sample through mechanisms such as adsorption on silicate surfaces (as described by Eq. (1)), cation exchange with K, or ion replacement in K-feldspar (microcline), leading to the formation of albite lamella within their structures. It is essential to note that some adsorption of Cl in the samples cannot be excluded. Remarkably, in the 10 wt% NaCl exposure, effluent Cl contents stabilize at approximately 50 g/L, slightly below the injected concentration, indicating a phenomenon of Cl removal from the fluids.

For the sample exposed to DW, effluent Na- and K-contents begin to decline following the injection of approximately 16 mL of water. This can be interpreted as the result of mixing and dilution of the in-situ pore fluid with injected water. However, the pH remains constant during this period, suggesting that pH might potentially be buffered by the release of OH^- from the sample. Additionally, there is a notable increase in Si content, suggesting the dissolution of a silicate phase at this stage. Subsequently, after the injection of about 26 mL, both Si-content and pH begin to decrease, suggesting at a possible depletion of one or more reactive phases. Taken together, these observations consistently highlight the requirement of an injection volume between 15 and 20 mL for the injected fluid to effectively pass the interconnected pore network.

For the GP-BR-10NaCl and GP-BR-15NaCl samples, the notable increases in effluent Cl-contents align closely with rises in effluent K-content, and (in the case of 10 wt% NaCl) decline in pH. This suggests a release of K^+ from the sample to counterbalance Cl^-. The decrease in pH may be attributed to the mixing of pore fluid (with a high pH) and brine (with a neutral pH). However, the initial effluent pH-values, as well as the concentrations of K and Si in these two samples, were notably lower compared to the other sample effluents. This observation challenges the current assumption and implies that the displaced initial pore fluid may have had a different composition.

Moreover, a distinct rise in effluent Si-content is consistently observed across all exposure tests, typically occurring at lower injected volumes than those required for Cl^- appearance. This further suggests that complete flushing of the pore network, accompanied by reactions releasing Si into the fluid (such as those enhancing the dissolution of quartz/amorphous silica in the presence of alkali ions, as outlined in path 3), had already occurred at this stage.

While a comprehensive understanding of the chemical interactions in our injection tests may be limited by the available data, notable observations emerge. These include Na^+ binding, accompanied by a release of K^+, particularly evident in samples exposed to high Cl-content fluids. Additionally, NaCl influences the augmented breakage of Si–O bonds in minerals, with heightened involvement of Ca ions in reactions, fostering increased (C,N,K)-A-S-H gel formation. This gel may further transform into zeolites via cation exchange, thereby enhancing Cl^- ion binding capacity.

4. Mechanistic insights into the impacts of brine exposure on GP system properties: an integrated analysis from micro to macro scales

To gain deeper insights into the main mechanisms behind the improved performance of GP systems when exposed to NaCl solutions, this section establishes a correlation between the microscale observations and the mechanical properties of the GP system. In summary, our findings challenge the simplistic notion that the improvement in compressive strength of GP systems following brine exposure can solely be attributed to reduced alkali leaching, as suggested in previous studies (see Table A1 in the Appendix). Instead, the results of SEM, XRD, BET, and FTIR analyses, complemented by the ICP-OES observations, reveal the following mechanisms being responsible for the enhanced mechanical performance of the GP samples tested here after exposure to NaCl-based brines:

- **Formation of Robust Gels and Secondary Minerals:** The presence of NaCl in the brine induces the formation of alkali-enriched (C,N,K)-A-S-H gels surrounding the reactive particles, which augments the strength and durability of the GP system. This has been supported by other research works [21,94]. NaCl prompts the contribution of Ca^{2+} ions into the reactions, triggering ion exchange processes, and subsequently leading to the formation of (C,N,K)-A-S-H and secondary minerals, such as zeolites. These transformations construct a highly interconnected geopolymeric network, through the formation of durable Si-O-T bonds. The system's increased capacity to adsorb Cl^- ions, particularly noticeable at higher NaCl concentrations, serves as additional confirmation of the heightened formation of (C,N,K)-A-S-H gels, aligning with prior literature findings [95,96].
- **Replacement of K-Feldspar by albite:** Exposure to NaCl-based brine facilitates dissolution-precipitation and fluid-assisted ion replacement processes within GP samples, potentially leading to the replacement of K-feldspar by albite. This precipitation of albite within the GP's microstructure may also contribute to the observed mechanical improvements.
- **Extended Reaction Duration:** The observed augmentation in the mechanical properties and permeability of the GP system may also be attributed, in part, to the prolonged reaction duration of these materials. Slower reaction kinetics may contribute to a continuous enhancement of material properties over extended periods.

The obtained results demonstrate the intricate interplay between microstructural changes and mechanical performance in brine-exposed GP systems, and provide valuable insights regarding the application of GP systems in challenging environments. However, it is crucial to note that the impact of NaCl ingress on different GP systems is subject to variations influenced by curing/exposure factors (e.g., NaCl concentration, curing/exposure temperature, etc.) and the initial GP system composition (including precursor type, alkali levels, mineralogical properties). This variability leads to conflicting outcomes documented in the literature (as shown in Table A1 in the Appendix). Consequently, different scenarios might cause distinct mechanisms, necessitating further research to unravel the unexplored aspects of NaCl's influence on GP systems.

5. Summary and concluding remarks

In this work, we assessed the alterations in mechanical properties and permeability of a geopolymer (GP) system specifically developed for CO_2-geosequestration upon exposure to deionized water (DW) and to brines with different concentrations of NaCl in the range 5–15 wt%. A dynamic-exposure technique using tri-axial experiments at 90 °C and 13.8 MPa was employed, forcing a flow of brine through a sample at set injection rates. After exposure, a comprehensive range of micro-scale analytical techniques was applied to analyse the link between the GP

system's permeability and mechanical properties, and its mineralogy, morphology, and chemical bonding, and to gain further insights into how these factors impact the system's stability. Key findings of this study are as follows:

- Mechanical Properties: Tri-axial experiments conducted at 90 °C and 13.8 MPa confining pressure revealed significant alterations in the mechanical properties of the GP system in response to varying NaCl concentrations in brines. Notably, a marked increase was observed in compressive strength, accompanied by elevated Young's moduli (though lower than those of OPC-based materials), and reduced Poisson's ratios in GP samples exposed to brines. These alterations may result in an elevated susceptibility to cracking in samples exposed to higher salinity levels, underscoring the importance of addressing associated risks, particularly when operating at elevated brine salinities.
- Permeability: Following the 3-week injection period, exposure led to a reduction in permeability across all GP samples, including the sample exposed to DW, compared to the reference sample. However, a clear impact of NaCl-content on permeability reduction was not observed. The permeability alterations appeared to be independent of the NaCl concentration of the brine, exhibiting a direct proportionality solely to the initial permeability of the samples.
- Effluent Analyses: During the three-week flooding period, initially high effluent pH decreased continuously in experiments using DW and low NaCl brine (5 wt%). Conversely, during experiments using higher NaCl concentrations (10 wt% and 15 wt%), effluent pH increased initially, followed by a subsequent decline. For all tests, there was a correlation between effluent pH and effluent Si-content. Furthermore, for experiments injecting NaCl-containing brine, effluents were consistently depleted of Na, while all effluents contained high concentrations of K. These observations are attributed to an interplay of chemical interactions, including silicate dissolution and hydrolysis, Na^+ adsorption and binding (supported by Cl^- trend), K-leaching, and the formation of alkali-enriched (C,N,K)-A-S-H gels and crystalline silicates.
- Micro-scale Analyses: SEM, XRD, FTIR, and BET analyses of fractured and powdered solid samples provided insights into the effects of DW and brine introduction on the GP system. DW resulted in reduced connectivity of the GP-network due to matrix dissolution and the formation of weak portlandite. In contrast, brine injection facilitated the formation of a robust network of alkali-enriched (C,N,K)-A-S-H gels, enhancing the strength and durability of GPs. NaCl-brine injection also induced the formation of secondary minerals (such as zeolites), and replacement of K-feldspars by albite through dissolution-precipitation processes, collectively reducing permeability and enhancing the overall performance of the GP system on both micro and macro scales. Extended reactions in the GP system, over the prolonged intervals, may also contribute to ongoing improvement in mechanical properties and permeability.

In summary, the results of this study highlight the effectiveness of the dynamic-exposure technique in understanding the interplay between brine salinity and GP system performance, with implications for optimizing their suitability in high-pressure, high-temperature downhole applications. While these findings contribute to advancing GP systems as dependable solutions for challenging environments, variations influenced by factors like ion type, ion concentration, temperature, and initial GP system composition warrant further research to uncover specific mechanisms and unexplored aspects of brines' impacts on GP systems. Additionally, the imposed-flow exposure method, while offering controlled assessments of GP behavior, has constraints, including its time-consuming nature and the requirement for specialized equipment, complicating test duplication and standard deviation measurement. Moreover, although XRD and SEM techniques offer valuable insights, their emphasis on crystallography and surface characteristics highlights the necessity for complementary methodologies in future studies. Techniques like Focused Ion Beam (FIB) and Transmission Electron Microscopy (TEM) are essential for enhancing analytical depth and achieving a comprehensive examination of structural changes across layers. Furthermore, although a NaCl-based brine was employed to facilitate result interpretation, it is crucial to note that formation waters in realistic geological formations consist of multiple ions beyond NaCl. The implications of these additional ions on GP properties necessitate further investigation in future studies.

CRediT authorship contribution statement

Seyed Hasan Hajiabadi: Writing – review & editing, Writing – original draft, Visualization, Validation, Software, Resources, Methodology, Investigation, Formal analysis, Data curation, Conceptualization. **Mahmoud Khalifeh:** Writing – review & editing, Validation, Supervision, Resources, Project administration, Methodology, Funding acquisition, Conceptualization. **Reinier van Noort:** Writing – review & editing, Validation, Supervision, Resources, Project administration, Methodology, Funding acquisition, Conceptualization.

Declaration of competing interest

The authors declare that they have no known competing financial interests or personal relationships that could have appeared to influence the work reported in this paper.

Data availability

Data will be made available on request.

Acknowledgement

The Authors acknowledge the CEMENTEGRITY project that is funded through the ACT program (Accelerating CCS Technologies, Horizon2020 Project No 691712). Financial contributions from the Research Council of Norway (RCN), the Netherlands Enterprise Agency (RVO), the Department for Energy Security & Net Zero (DESNZ, UK), and Wintershall DEA are gratefully acknowledged.

The authors also extend their sincere gratitude to Mr. Ingar Johansen from the Institute of Energy Technology (IFE) for his invaluable contribution to the analysis of effluents using ICP-OES and HR-ICP-MS.

Appendix

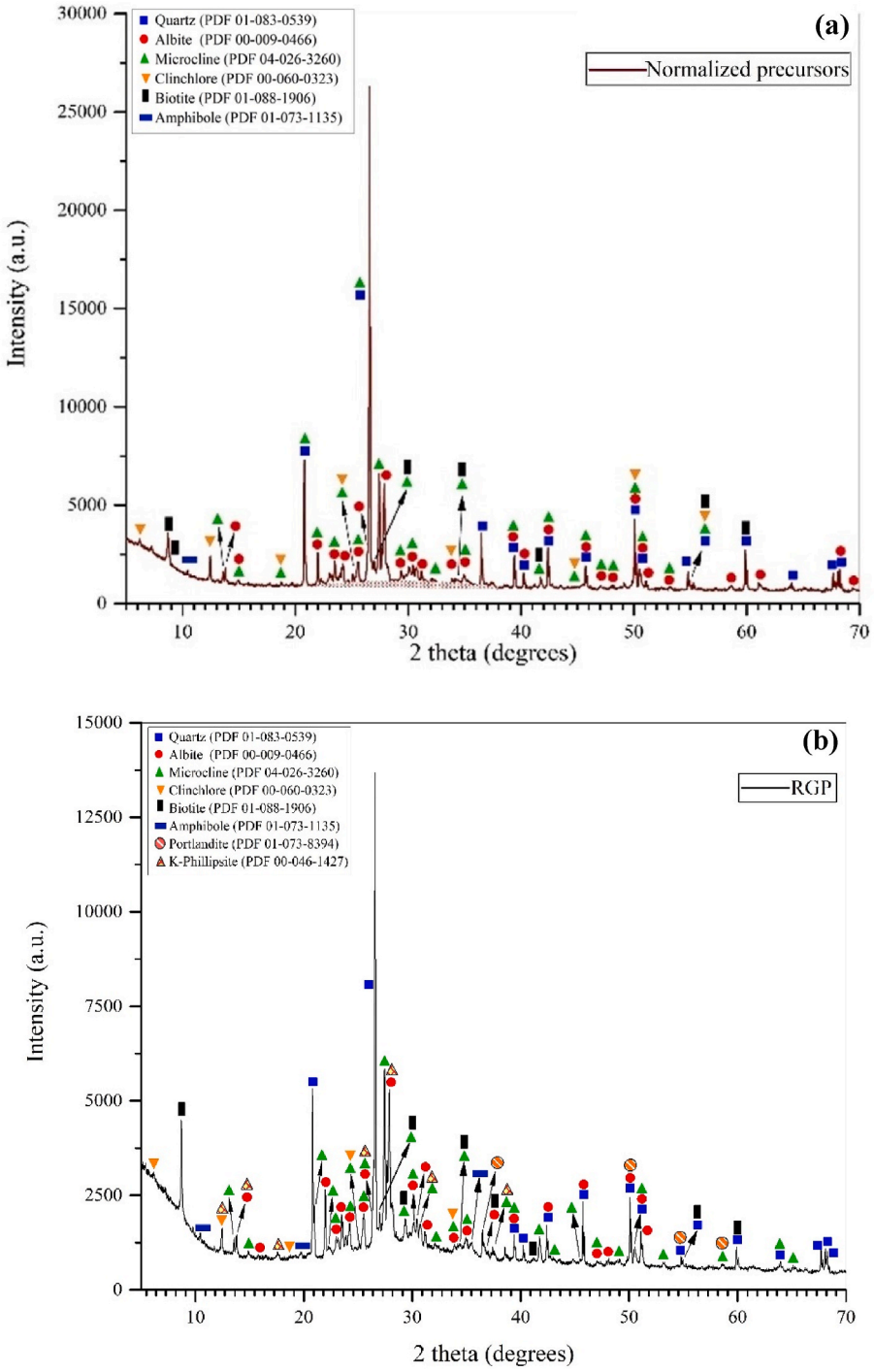

Fig. A1. XRD analysis of normalized precursors (a), and GP samples, including RGP (b), GP-DW-0NaCl (c), GP-BR-5NaCl (d), GP-BR-10NaCl (e), and GP-BR-15NaCl (f) after three-week exposure period at simulated downhole conditions.

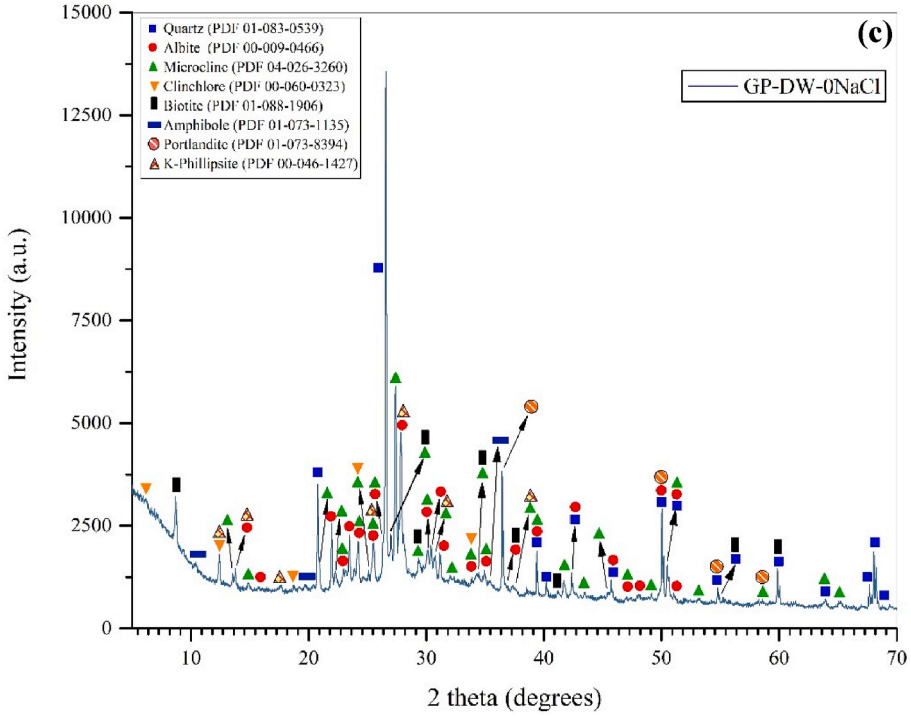

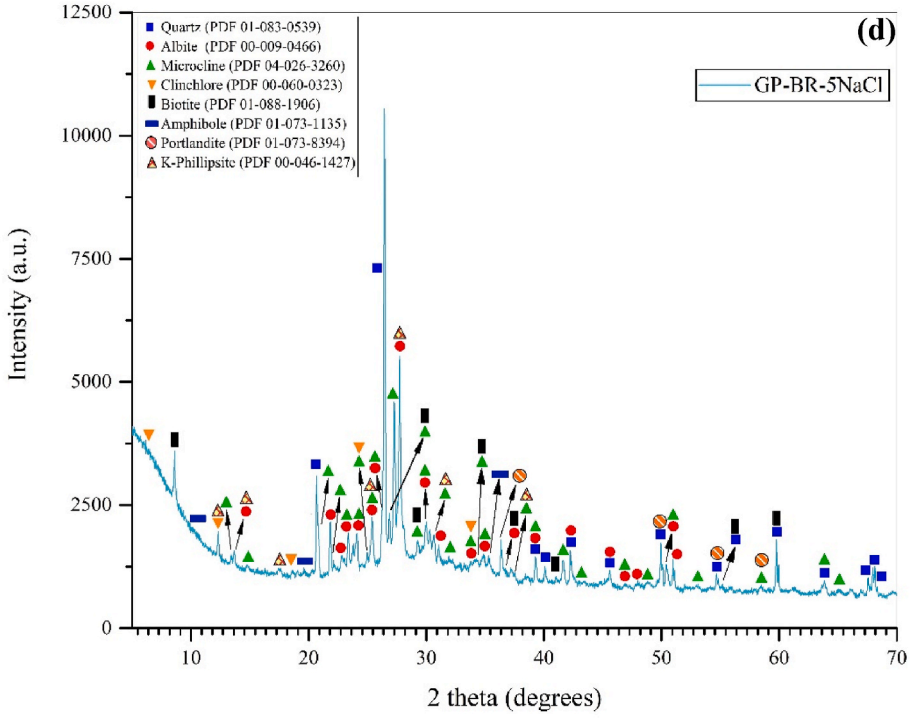

Fig. A1. (*continued*).

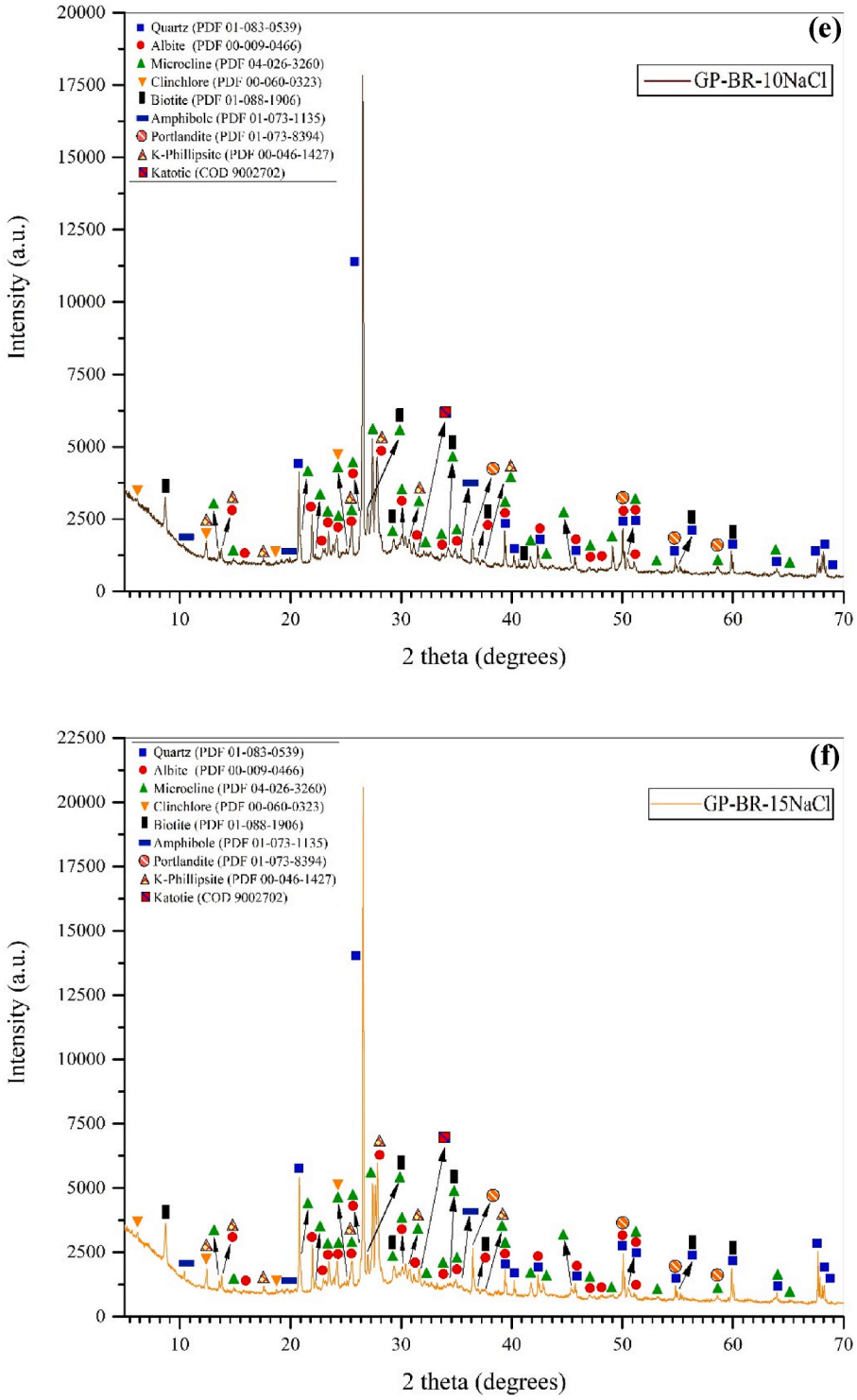

Fig. A1. (*continued*).

Table A1
A list of published studies on GP/cement systems exposed to brines or chemicals simulating Na^+, Cl^- attack, or hydrothermal treatment of GPs.

Author(s)	Aim (s)	Materials (Precursors)	Experimental Conditions/Methods	Main achievement(s)
Mohamed, Ranjith and Sanjayan [97]	To evaluate the mechanical properties of GP cement immersed in low (5% NaCl) and high (15% NaCl) brine solutions.	- FFA	-Static exposure for 14, 30, 60, and 90 days. -Assessing brine's impact on strength, crack propagation, and strain over time.	-GP strength diminishes in NaCl brine, with higher NaCl concentration slowing the reduction rate. -Failure strain decreases upon brine introduction.

(*continued on next page*)

Table A1 (*continued*)

Author(s)	Aim (s)	Materials (Precursors)	Experimental Conditions/Methods	Main achievement(s)
				-Higher NaCl concentrations are preferable for GP cement in CCS applications.
Khalifeh, Todorovic, Vrålstad, Saasen and Hodne [41]	To examine the durability of rock-based GPs in harsh conditions, including crude oil, brine, and H_2S in brine.	- Aplite rock - Slag - Micro-silica	GPs were cured at room temperature for one week, then exposed to 2.45% NaCl (plus oil and H_2S) at 100 °C for up to 12 months.	-GPs showed low permeability after brine exposure, with compressive strength rising after six months. -However, H_2S-exposed samples suffered severe degradation.
Ren, Yan, Duan, Zhang, Li and Yan [32]	To evaluate the durability of MK-based GPs reinforced with wollastonite, tremolite, and short basalt fiber when exposed to Na_2SO_4 and NaCl solutions.	- MK - Wollastonite - Short basalt fibre - Tremolite	GPs were immersed in NaCl (0–20 wt %) and Na_2SO_4 (5–20%) solutions at 28 °C for 3, 7, 28, and 90 days.	-The compressive strength reduction from NaCl and Na_2SO_4 exposure increased with time due to microcrack development. -Na_2SO_4 exposure resulted in more pronounced cracks and higher porosity than NaCl.
Nasvi, Ranjith, Sanjayan, Haque and Li [30]	To explore the impact of varying NaCl concentrations on the mechanical properties of wellbore materials.	- FFA - OPC - Sandstone	Samples were cured in 5% and 15% NaCl solutions for 24 h at 50 °C.	GPs exhibited approximately half strength reduction compared to OPC, owing to decreased alkali leaching.
Prusty and Pradhan [44]	To study the influence of chloride on the properties of GP concrete in marine conditions.	- FFA - Slag	-GPs were made by mixing FFA and slag with 0 and 3.5 wt% of NaCl. -Curing involved 48 h at room temperature followed by 48 h at 80 °C.	-FFA-Slag-based GPs initially had higher strength than FFA-based GPs. -A 7.86% decrease in FA-based GPs and a 30.24% decline in FA-slag-based ones were attributed to salt crystallization impacts.
Duguid, Radonjic and Scherer [98]	To evaluate the rate of cement degradation caused by carbonated brine penetrating reservoir rocks.	- Class H cement	-A year-long study exposed Class H cement in sandstones and limestones, typical CCS reservoir rocks, to brines, at temperatures of 20 °C and 50 °C. -Analysis was conducted at 1, 2, 3, 6, and 12-month intervals.	-Limestone-embedded cements resisted degradation. -Sandstone samples degraded rapidly, especially under low pH conditions. -Pozzolans and additives could help mitigate degradation.
Pan, Wu and Huang [99]	To investigate the prolonged strength development of MgO-slag paste during brine curing.	- MgO activated slag - OPC	The MgO-slag samples were immersed in single salt and mixed double-salt solutions of ions (NaCl, Na_2SO_4, $MgCl_2$, $MgSO_4$) for one year.	-MgO-activated slag lost strength rapidly after 150 days in brine solutions. -Corrosion damage was more pronounced with $SO_4^{2-} > Cl^- $ and $Mg^{2+} > Na^+$ ions. -Strength decline stemmed from CSH depletion in acidic solutions and expansive AFt formation (ettringite-like phases) in SO_4^{2-} solutions.
Ridha, Abd Hamid and Che Ku Mazuan [100]	To investigate changes in the mechanical properties of GP cement with different brine salinity levels.	- FFA - Class G cement	Samples were cured at 130 °C and 3000 psi for 24 h, then immersed in brine with up to 30% NaCl for 28 days	The GP experienced strength reduction in brine, but the rate was roughly half that of OPC.
Abdoulghafour, Luquot and Gouze [101]	To assess the impact of fractured well cement degradation on leakage rate under CCS conditions.	- Class G cement	Monitoring permeability during the flow of CO_2-enriched brine through a single fracture in a class G cement core.	-Initial fracture leakage can self-mitigate via alteration product development and cement carbonation. -Silica-rich layer formation governs permeability, influenced by pH and cement interactions. -Amorphous silica-rich material notably reduced CO_2 leakage through fractures.
Gonzalez-Estrella, Ellison, Stormont, Shaikh, Peterson, Lichtner and Cerrato [102]	To study the impact of saline brine on fractured wellbore cement.	- Cement	Varying hydrostatic confining pressures were applied in flow experiments, reacting sequentially with nitrogen, de-ionized water, and brine ($CaCl_2$, NaCl, $NaHCO_3$ mixture).	Brine injection, especially when supersaturated with $CaCO_3$, reduces fracture aperture, thereby mitigating the risk of leakage.
Yan, Wei, Muchiri, Li, Zhang and Xu [103]	To study cement response to CO_2-saturated brine.	- Class G cement blended with silica fume, liquid silica, and latex	Samples were subjected to exposure to high temperature (150 °C) and high partial pressure of CO_2-saturated brine	-Brine exposure significantly affected the cement's mechanical properties. -The admixtures used created a dense C–S–H crystal structure, reducing cement permeability and enhancing resistance to CO_2-brine corrosion.
Samarakoon, Ranjith and Wanniarachchi [104]	To assess carbonation effects on alkali-activated cement (AAC) versus OPC in subsurface conditions.	- Class G cement - FFA - Slag	Exposing various AAC compositions and OPC to carbonated brine for 28 days.	AACs, particularly those with elevated Ca content due to slag addition, showed advantages over OPC in resisting carbonation and improving mechanical properties.
Ozyurtkan and Radonjic [105]	To assess mineralogical and microstructural changes in cements	- Class H cement	-Salt solution comprised NaCl and KCl.	-Fracture development increased hydraulic conductivity after 100 days.

(*continued on next page*)

Table A1 (*continued*)

Author(s)	Aim (s)	Materials (Precursors)	Experimental Conditions/Methods	Main achievement(s)
	with fractures after exposure to CO_2-rich brine flow.		-CO_2-equilibrated brine with a pH range of 4.9–5.2 was used for the flow-through experiment. -CO_2-saturated brine flowed at 2 ml/min, with a confining pressure of 600 psi.	-Acidic brine contact raised porosity, with secondary fractures amplifying changes. -A decrease in porosity was observed, possibly due to mineral deposition and pore plugging influenced by carbonation.
Thirumakal, Nasvi and Sinthulan [55]	To evaluate the mechanical behaviour of GP and OPC in different downhole conditions.	- FFA - High sulfate resistance OPC	GP and OPC samples were immersed in saline water with NaCl contents ranging from 0% to 30% for 45 days.	-GP's strength increased with salinity, showing better resistance to alkali leaching than OPC (6–66% higher UCS). -OPC's strength peaked at 10% NaCl, then declines with higher levels.
Giasuddin, Sanjayan and Ranjith [52]	To assess the effectiveness of GP cement curing in saline water in comparison to OPC, pertinent to CCS applications in aquifers.	- FFA - Slag - OPC	After curing, samples were immersed in 0%, 8%, and 15% NaCl solutions for 28 days.	In saline water curing, GPs had higher compressive strengths due to reduced alkali leaching, while OPCs showed a sharp decline in strength.
Kang and Kim [106]	To evaluate a calcium sulfoaluminate (CSA) and slag blend as eco-friendly cement and exploring innovative applications for waste brine from seawater desalination.	- CSA - Slag	-CSA content varied at 0%, 10%, 20%, and 30% substitution levels. -Water mixtures included freshwater and brine.	Brine enhances the hydration reaction of CSA in blended cement, resulting in the formation of ettringite and influencing pore content.
Tittarelli, Mobili, Giosuè, Belli and Bellezze [46]	To investigate steel reinforcement corrosion in geopolymeric and cementitious mortars exposed to 3.5% NaCl solution.	- FFA - MK - OPC	-Embedding steel reinforcements in GP and OPC-based mortars of different strengths. -The specimens undergo curing and exposure to wet-dry cycles in a 3.5% NaCl solution.	-High alkalinity in GPs prolonged the active state of steel during curing. -FFA-based GPs provided better protection to bare steel compared to MK-based GPs (with higher porosity). -Geopolymeric matrices altered the minimum chloride threshold for corrosion initiation.
Lee and Van Deventer [107]	To analyse the interface between natural siliceous aggregates and FFA-based GPs and to examine the effect of chloride contamination (KCl) on interfacial bonding strength.	- Natural siliceous aggregates - FFA	-Activating solutions comprised various soluble silicate concentrations and KCl. -Evaluation focused on microstructure and bonding strength at the aggregate-GP interface.	-Soluble silicates enhance bonding in GPs. -Higher dosage results in stronger interfaces and denser binders. -Chloride contamination weakens bonding, affecting mortar and concrete strength.
Zhang, Yao and Wang [108]	To study the potential applications of GP coatings for marine concrete structures, particularly their anti-corrosion behaviour and bonding strength to cement.	- GPs synthesized with 90% MK and 10% slag. - OPC	Investigated the interfaces between GP and cement paste/mortar, and pore structure of GP.	GPs exhibited excellent anticorrosion properties and efficient bonding to cement paste due to their compact microstructure, smaller pores compared to OPC, and chemical stability in sea water or air.
Tennakoon, Shayan, Sanjayan and Xu [109]	To analyse chloride permeability and corrosion initiation in GP concrete for structural applications.	- FFA - Slag - OPC	GP and OPC concrete underwent accelerated chloride exposure (2%), with corrosion initiation in embedded rebar monitored.	-GP concrete outperforms OPC in chloride diffusion and corrosion resistance. -Higher slag content delays chloride-induced corrosion and enhances protection against reinforced corrosion.
Chindaprasirt and Chalee [110]	To study the performance of high-calcium FFA-based GP in chloride diffusion, aging resistance, and corrosion initiation time.	- CFA-based GP concrete samples with varying concentrations of NaOH and slag content.	Exposure of samples to seawater for a period of three years.	Increased NaOH concentration leads to faster strength gain, reduced chloride ingress (reduced chloride binding) and reduced steel corrosion in GP.
Keleştemur and Demirel [111]	To explore the influence of varying cement substitution ratios with MK on the properties, and corrosion behaviour of structural lightweight concrete (SLC) specimens.	- SLC - MK	-SLC specimens were prepared with varying MK ratios (5%, 10%, 15%, and 20% w/w). -Reinforcing steel bars were embedded in the SLC specimens.	MK enhanced the mechanical properties of SLC, with 15% w/w exhibiting optimal strength development, improved corrosion resistance, and superior microstructure.
Ganesan, Abraham and Raj [112]	To assess the durability of plain and fiber-reinforced GP concrete in comparison to OPC concrete.	- FFA - OPC	Cured specimens underwent durability testing (water absorption, sorptivity, etc.) after being cured at 60 °C for 24 h and air-dried for 24 h.	GP concrete, both plain and fiber reinforced, showed superior durability compared to OPC concrete, especially in water absorption, abrasion resistance, and resistance to chloride, acid, and sulfate attack.
Vafaei, Allahverdi, Dong and Bassim [113]	To examine the durability of GP cement mortar with waste-glass powder and calcium aluminate cement in acid exposure.	- Waste-glass based GP - OPC (control sample) - High alumina cement (control sample)	Monitoring compressive strength and mass loss at different time intervals (over 24 months) of exposure to HCl and H_2SO_4.	-GP outperformed control mortars in acid solutions, with minimal losses in mass and compressive strength. -GP cement's durability is due to its stable aluminosilicate structure and low calcium content. -H_2SO_4 caused faster degradation than HCl in GP due to gypsum crystal formation, resulting in cracking and spalling.
Gunasekara, Law, Bhuiyan, Setunge and Ward [45]	To study reinforcement corrosion resistance in GP concrete versus OPC	- Three different FFAs - OPC for comparison	Subject specimens to wet-dry cycles and ponding in 3% NaCl solution.	-GP concrete corrodes faster than OPC concrete due to geopolymerization and pH reduction.

(*continued on next page*)

Table A1 (*continued*)

Author(s)	Aim (s)	Materials (Precursors)	Experimental Conditions/Methods	Main achievement(s)
	concrete under different chloride exposure conditions.			-Chloride diffusion in GP concrete is influenced by porosity. -The CaO content in GP concrete affects chloride binding capacity by producing C–A–S–H gel, which adsorbs chloride ions, reducing ingress.
Javed, Shaikh and Sarker [114]	To study the influence of silica fume on strength loss in lithium slag GP (LSG) mortars after strong acid exposure.	- LSG mortars containing sodium (Na) and potassium (K) based alkaline activators.	The mortars were exposed to 5% sulphuric and hydrochloric acid solutions separately for 60 days.	-Na-activated LSGs resist acids better than K-activated ones. -Silica fume densifies the microstructure, reducing strength loss in acidic conditions. -Microstructural analysis shows calcium sulfate crystal formation and aluminum leaching, deteriorating the aluminosilicate gel.
Mayhoub, Mohsen, Alharbi, Abadel, Habib and Kohail [115]	To study the impact of curing conditions on compressive strength and chloride binding capacity of FFA-based GP pastes with varying chloride levels.	- FFA	-Preparation of FFA GP pastes with different chloride contents (1%, 2%, and 4%). -Application of different curing regimes: normal, oven, steam, and microwave.	-Thermal curing enhanced the geopolymerization process, reduced unreacted grains, promoted a denser microstructure, and reduced chloride ingress. -Increased humidity during curing led to a compact microstructures and enhanced chloride binding capacity.
Pasupathy, Sanjayan, Rajeev and Law [116]	To assess durability of slag-based GP concrete in marine spray/splash zones, compared to OPC.	- FFA - OPC - Coarse and fine aggregates	Slag-based GP and OPC concrete blocks were placed in a marine environment in southern Australia, each with steel bars at specific depths.	GP exhibited higher porosity, increased susceptibility to chloride penetration, greater scaling effect, and higher vulnerability to sulfate attack compared to OPC.
He, Li, Meng and Shen [117]	To analyse the impact of NaCl and gypsum on slag-based GP concrete activated by quicklime.	- Slag	Various combinations of NaCl and gypsum were added to the GP concrete mixtures to observe their effects.	-NaCl and gypsum increased GP's compressive strength and significantly improved sulfate corrosion resistance. -NaCl and gypsum combination led to the generation of Friedel's salt, Kuzel's salt, and NaOH, further enhancing strength.
Nastiti and Ekaputri [118]	To evaluate the impact of chloride ions on OPC concrete coated with FFA-based GP mortar, especially in coastal areas	- FFA - OPC	Coatings of varying thickness (2.5 cm, 4 cm, and 6 cm) were applied to OPC concrete, exposed to a marine environment with seawater curing for 90 days.	-Coating OPC concrete with GP enhanced compressive strength in seawater, with a 4 cm thickness recommended for optimal performance. -The coating effectively binds chloride ions, preventing their ingress into sound concrete.
He, Wang, Fu, Wang, Zhao, Liu, Jiang, Jia and Zhou [119]	To develop a method to produce bulk zeolites with adjustable properties for efficient adsorption of hazardous elements.	- MK	Varying hydrothermal conditions and initial Na/K ratios were applied to control phase compositions.	-Analcime formation from GP was facilitated by alkaline conditions and high temperature. -Zeolite phase compositions tailored by adjusting Na/K ratio. -GP and resulting zeolite adsorbed Cs^{+} and Sr^{2+} via ion exchange and chemisorption.
Yan, Xue-min, Liu, Liu and Chen [120]	To assess the potential of hydrothermal transformation of GPs into self-supporting zeolites.	- Amorphous Al_2O_3–SiO_2 powder combined with DW or silicate solutions.	GP samples were synthesized via a sol-gel method, then cured at 60 °C for 24 h and hydrothermally treated at 90 °C for 6 h.	-Geopolymerization can induce zeolite nucleation with proper Si/Al ratio, water usage, and reaction conditions. -Hydrothermal transformation of Al_2O_3–$2SiO_2$–Na_2O GPs yielded NaA zeolites. -Similar coordination structures were found in Al_2O_3–$2SiO_2$–Na_2O GPs and NaA zeolites.
Yang, Zhang, Fu, Hou and Dong [121]	To investigate the impact of alkaline hydrothermal activation on Molybdenum tailings (MT) reactivity and mechanical properties of the resulting one-part GP.	- MT - Slag	-Alkaline hydrothermal activation was conducted on MT to promote silicon dissolution and alter its structure. -One-part GPs were then prepared by adding water to activated MT and slag.	-Alkaline hydrothermal activation enhanced silicon dissolution and modified quartz properties in MT, forming amorphous sodium aluminosilicate. -This altered MT morphology, increasing its chemical activity and improving resulting GP's mechanical properties.
Khalid, Lee, Park, Abbas and Lee [122]	To propose a one-step hydrothermal method for synthesizing GP-supported zeolites from industrial by-products as adsorbents.	- FFA - Slag	Different synthesis conditions and parameters such as hydrothermal treatment time, temperature/ pressure, and slag content were investigated.	-Higher slag content favoured compressive strength development but decreased zeolite content and BET surface area. -GP-supported zeolites exhibited higher volume of mesopores, crucial for adsorption capacity.
Murayama, Yamamoto and Shibata [123]	To study the mechanism of zeolite synthesis from coal FFA via hydrothermal reactions in different alkali solutions.	- FFA	Conducted hydrothermal reactions in an autoclave to synthesize zeolite from coal FFA.	-Zeolite P and chabazite were primarily synthesized from coal FFA.

(*continued on next page*)

Table A1 (*continued*)

Author(s)	Aim (s)	Materials (Precursors)	Experimental Conditions/Methods	Main achievement(s)
			Examined changes in physical and chemical properties of the obtained zeolites.	-Alkali hydrothermal reaction involved three steps: Si^{4+} and Al^{3+} dissolution, condensation of silicate and aluminate ions to form aluminosilicate gel, and zeolite crystallization. -OH^- aided Si^{4+} and Al^{3+} dissolution, while Na^+ facilitated zeolite P crystallization. -Na^+ concentration predominantly controlled zeolite synthesis rate. -Crystallization rate decreased with increasing K^+ concentration in the presence of Na^+.

FFA: Class-F Fly ash CFA: Class-C Fly ash MK: Metakaolin.

References

[1] R.E. Hester, R.M. Harrison, Carbon Capture: Sequestration and Storage, Royal Society of Chemistry, 2010.
[2] S. Iglauer, A.Z. Al-Yaseri, R. Rezaee, M. Lebedev, CO2 wettability of caprocks: implications for structural storage capacity and containment security, Geophys. Res. Lett. 42 (21) (2015) 9279–9284.
[3] S.H. Hajiabadi, P. Bedrikovetsky, S. Borazjani, H. Mahani, Well Injectivity during CO2 Geosequestration: A Review of Hydro-Physical, Chemical, and Geomechanical Effects, Energy & Fuels, 2021.
[4] S. Taku Ide, K. Jessen, F.M. Orr, Storage of CO2 in saline aquifers: effects of gravity, viscous, and capillary forces on amount and timing of trapping, Int. J. Greenh. Gas Control 1 (4) (2007) 481–491.
[5] S. Iglauer, Dissolution Trapping of Carbon Dioxide in Reservoir Formation Brine-A Carbon Storage Mechanism, INTECH Open Access Publisher, 2011.
[6] R. Miri, R. van Noort, P. Aagaard, H. Hellevang, New insights on the physics of salt precipitation during injection of CO2 into saline aquifers, Int. J. Greenh. Gas Control 43 (2015) 10–21.
[7] R. Miri, H. Hellevang, Salt precipitation during CO2 storage—a review, Int. J. Greenh. Gas Control 51 (2016) 136–147.
[8] M. Burton, N. Kumar, S.L. Bryant, CO2 injectivity into brine aquifers: why relative permeability matters as much as absolute permeability, Energy Proc. 1 (1) (2009) 3091–3098.
[9] A. Raza, R. Rezaee, R. Gholami, V. Rasouli, C.H. Bing, R. Nagarajan, M.A. Hamid, Injectivity and quantification of capillary trapping for CO2 storage: a review of influencing parameters, J. Nat. Gas Sci. Eng. 26 (2015) 510–517.
[10] H. Jung, D.N. Espinoza, S.A. Hosseini, Wellbore injectivity response to step-rate CO2 injection: coupled thermo-poro-elastic analysis in a vertically heterogeneous formation, Int. J. Greenh. Gas Control 102 (2020) 103156.
[11] P.B. Kelemen, J. Matter, E.E. Streit, J.F. Rudge, W.B. Curry, J. Blusztajn, Rates and mechanisms of mineral carbonation in peridotite: natural processes and recipes for enhanced, in situ CO2 capture and storage, Annu. Rev. Earth Planet Sci. 39 (2011) 545–576.
[12] P. Roy, J.P. Morris, S.D. Walsh, J. Iyer, S. Carroll, Effect of thermal stress on wellbore integrity during CO2 injection, Int. J. Greenh. Gas Control 77 (2018) 14–26.
[13] J. Choo, W. Sun, Cracking and damage from crystallization in pores: coupled chemo-hydro-mechanics and phase-field modeling, Comput. Methods Appl. Mech. Eng. 335 (2018) 347–379.
[14] L.K. Turner, F.G. Collins, Carbon dioxide equivalent (CO2-e) emissions: a comparison between geopolymer and OPC cement concrete, Construct. Build. Mater. 43 (2013) 125–130.
[15] M. Zhang, S. Bachu, Review of integrity of existing wells in relation to CO2 geological storage: what do we know? Int. J. Greenh. Gas Control 5 (4) (2011) 826–840.
[16] A. Duguid, An estimate of the time to degrade the cement sheath in a well exposed to carbonated brine, Energy Proc. 1 (1) (2009) 3181–3188.
[17] V. Barlet-Gouedard, G. Rimmelé, B. Goffé, O. Porcherie, Well technologies for CO2 geological storage: CO2-resistant cement, Oil Gas Sc. Tech.-Revue de l'IFP 62 (3) (2007) 325–334.
[18] V. Barlet-Gouédard, G. Rimmelé, O. Porcherie, N. Quisel, J. Desroches, A solution against well cement degradation under CO2 geological storage environment, Int. J. Greenh. Gas Control 3 (2) (2009) 206–216.
[19] E. Lécolier, A. Rivereau, G. Le Saoût, A. Audibert-Hayet, Durability of hardened portland cement paste used for oilwell cementing, Oil Gas Sc. Tech.-Revue de l'IFP 62 (3) (2007) 335–345.
[20] S. Salehi, C.P. Ezeakacha, M. Khattak, Geopolymer Cements: How Can You Plug and Abandon a Well with New Class of Cheap Efficient Sealing Materials, SPE Oklahoma City Oil and Gas Symposium, OnePetro, 2017.
[21] S.H. Hajiabadi, M. Khalifeh, R. van Noort, P.H. Silva Santos Moreira, Review on Geopolymers as Wellbore Sealants: State of the Art Optimization for CO2 Exposure and Perspectives, ACS Omega, 2023.
[22] X. Ge, X. Hu, H. Li, C. Shi, Synergistic effect of characteristics of raw materials on controlling the mechanical properties of fly ash-based geopolymers, Cement Concr. Compos. 145 (2024) 105368.
[23] J. Davidovits, Geopolymer Cement, A Review, Geopolymer Institute, 2013, pp. 1–11. Technical papers 21.
[24] M. Nadeem, S. Ilyas, E.U. Haq, F. Ahmed, M. Zain-ul-Abdein, M.R.A. Karim, S.F. A. Zaidi, Improved water retention and positive behavior of silica based geopolymer utilizing granite powder, Silicon (2021) 1–13.
[25] F. Li, Q. Chen, Y. Lu, Y. Zou, S. Li, Mitigating drying shrinkage and enhancing mechanical strength of fly ash-based geopolymer paste with functionalized MWCNTs grafted with silane coupling agent, Cement Concr. Compos. 143 (2023) 105250.
[26] T.H. Vu, N. Gowripalan, P. De Silva, A. Paradowska, U. Garbe, P. Kidd, V. Sirivivatnanon, Assessing carbonation in one-part fly ash/slag geopolymer mortar: change in pore characteristics using the state-of-the-art technique neutron tomography, Cement Concr. Compos. 114 (2020) 103759.
[27] Z. Yao, X. Ji, P. Sarker, J. Tang, L. Ge, M. Xia, Y. Xi, A comprehensive review on the applications of coal fly ash, Earth Sci. Rev. 141 (2015) 105–121.
[28] L. Tchadjié, J. Djobo, N. Ranjbar, H. Tchakouté, B.D. Kenne, A. Elimbi, D. Njopwouo, Potential of using granite waste as raw material for geopolymer synthesis, Ceram. Int. 42 (2) (2016) 3046–3055.
[29] L. Zhang, S. Ahmari, J. Zhang, Synthesis and characterization of fly ash modified mine tailings-based geopolymers, Construct. Build. Mater. 25 (9) (2011) 3773–3781.
[30] M.C.M. Nasvi, P.G. Ranjith, J. Sanjayan, A. Haque, X. Li, Mechanical behaviour of wellbore materials saturated in brine water with different salinity levels, Energy 66 (2014) 239–249.
[31] M. Nasvi, T. Rathnaweera, E. Padmanabhan, Geopolymer as well cement and its mechanical integrity under deep down-hole stress conditions: application for carbon capture and storage wells, Geomech. Geophys. Geo-Energy Geo-Resour. 2 (4) (2016) 245–256.
[32] D. Ren, C. Yan, P. Duan, Z. Zhang, L. Li, Z. Yan, Durability performances of wollastonite, tremolite and basalt fiber-reinforced metakaolin geopolymer composites under sulfate and chloride attack, Construct. Build. Mater. 134 (2017) 56–66.
[33] M. Muraleedharan, Y. Nadir, Factors affecting the mechanical properties and microstructure of geopolymers from red mud and granite waste powder: a review, Ceram. Int. 47 (10) (2021) 13257–13279.
[34] P. Nuaklong, P. Worawatnalunart, P. Jongvivatsakul, S. Tangaramvong, T. Pothisiri, S. Likitlersuang, Pre-and post-fire mechanical performances of high calcium fly ash geopolymer concrete containing granite waste, J. Build. Eng. 44 (2021) 103265.
[35] M. Okrusch, H.E. Frimmel, Mineralogy: an Introduction to Minerals, Rocks, and Mineral Deposits, Springer Nature, 2020.
[36] C. Klein, A.R. Philpotts, Earth Materials: Introduction to Mineralogy and Petrology, Cambridge University Press, 2013.
[37] S.H. Hajiabadi, M. Khalifeh, R. van Noort, Multiscale insights into mechanical performance of a granite-based geopolymer: unveiling the micro to macro behavior, Geoenergy Sci. Eng. 231 (2023) 212375.
[38] S. Nath, S. Kumar, Influence of iron making slags on strength and microstructure of fly ash geopolymer, Construct. Build. Mater. 38 (2013) 924–930.
[39] M. Khalifeh, A. Saasen, H. Hodne, R. Godøy, T. Vrålstad, Geopolymers as an alternative for oil well cementing applications: a review of advantages and concerns, J. Energy Resour. Technol. 140 (9) (2018).
[40] S. Hajiabadi, M. Khalifeh, R. Van Noort, P.S.S. Moreira, Effect of Magnesium-Bearing Additives on the Properties of a Granite-Based Geopolymer Sealant for CCS, 84th EAGE Annual Conference & Exhibition, European Association of Geoscientists & Engineers, 2023, pp. 1–5.
[41] M. Khalifeh, J. Todorovic, T. Vrålstad, A. Saasen, H. Hodne, Long-term durability of rock-based geopolymers aged at downhole conditions for oil well cementing operations, J. Sustain. Cement-Based Mater. 6 (4) (2017) 217–230.
[42] M. Khalifeh, A. Saasen, H.B. Larsen, H. Hodne, Development and characterization of norite-based cementitious binder from an ilmenite mine waste stream, Adv. Mater. Sci. Eng. (2017) 2017.
[43] J.L. Provis, J.S.J. Van Deventer, Geopolymers: Structures, Processing, Properties and Industrial Applications, Elsevier, 2009.

[44] J.K. Prusty, B. Pradhan, Effect of GGBS and chloride on compressive strength and corrosion performance of steel in fly ash-GGBS based geopolymer concrete, Mater. Today: Proc. 32 (2020) 850–855.
[45] C. Gunasekara, D. Law, S. Bhuiyan, S. Setunge, L. Ward, Chloride induced corrosion in different fly ash based geopolymer concretes, Construct. Build. Mater. 200 (2019) 502–513.
[46] F. Tittarelli, A. Mobili, C. Giosuè, A. Belli, T. Bellezze, Corrosion behaviour of bare and galvanized steel in geopolymer and Ordinary Portland Cement based mortars with the same strength class exposed to chlorides, Corrosion Sci. 134 (2018) 64–77.
[47] H. Zhu, Z. Zhang, Y. Zhu, L. Tian, Durability of alkali-activated fly ash concrete: chloride penetration in pastes and mortars, Construct. Build. Mater. 65 (2014) 51–59.
[48] M. Khalifeh, A. Saasen, T. Vrålstad, H.B. Larsen, H. Hodne, Experimental study on the synthesis and characterization of aplite rock-based geopolymers, J. Sustain. Cement-Based Mater. 5 (4) (2016) 233–246.
[49] H.M. Khater, Effect of silica fume on the characterization of the geopolymer materials, Int. J. Advan. Struct. Eng. 5 (1) (2013) 1–10.
[50] L.N. Assi, E.E. Deaver, P. Ziehl, Using sucrose for improvement of initial and final setting times of silica fume-based activating solution of fly ash geopolymer concrete, Construct. Build. Mater. 191 (2018) 47–55.
[51] M.A.A. Alvi, M. Khalifeh, M.B. Agonafir, Effect of nanoparticles on properties of geopolymers designed for well cementing applications, J. Petrol. Sci. Eng. 191 (2020) 107128.
[52] H.M. Giasuddin, J.G. Sanjayan, P.G. Ranjith, Strength of geopolymer cured in saline water in ambient conditions, Fuel 107 (2013) 34–39.
[53] Y. Wang, X. Liu, W. Zhang, Z. Li, Y. Zhang, Y. Li, Y. Ren, Effects of Si/Al ratio on the efflorescence and properties of fly ash based geopolymer, J. Clean. Prod. 244 (2020) 118852.
[54] S. Ridha, A.I. Abd Hamid, C.K.A.H.C. Ku, Influence of different brine water salinity on mechanical properties of fly ash-based geopolymer cement, Int. J. Struct. Integrity (2018).
[55] P. Thirumakal, M. Nasvi, K. Sinthulan, Comparison of mechanical behaviour of geopolymer and OPC-based well cement cured in saline water, SN Appl. Sci. 2 (8) (2020) 1–17.
[56] F. Chamssine, L.H. Gasparotto, M.A.F. Souza, M. Khalifeh, J.C. de Oliveira Freitas, Retarding mechanism of Zn2+ species in geopolymer material using Raman spectroscopy and DFT calculations, Sci. Rep. 12 (1) (2022) 1–9.
[57] F. Chamssine, M. Khalifeh, A. Saasen, Effect of Zn2+ and K+ as retarding agents on rock-based geopolymers for downhole cementing operations, J. Energy Resour. Technol. 144 (5) (2022) 053002.
[58] A. Rp, Recommended practice for testing well cements, API RECOMMEND. PRACT. 2 (2013) 10B.
[59] R. Api, API TR 10TR7, Mechanical Behavior of Cement, 2017.
[60] S.H. Hajiabadi, H. Aghaei, M. Kalateh-Aghamohammadi, A. Sanati, A. Kazemi-Beydokhti, F. Esmaeilzadeh, A comprehensive empirical, analytical and tomographic investigation on rheology and formation damage behavior of a novel nano-modified invert emulsion drilling fluid, J. Petrol. Sci. Eng. 181 (2019) 106257.
[61] M. Nasvi, P. Ranjith, J. Sanjayan, H. Bui, Effect of temperature on permeability of geopolymer: a primary well sealant for carbon capture and storage wells, Fuel 117 (2014) 354–363.
[62] D. Norsok, D-010 Well Integrity in Drilling and Well Operations, Standards Norway, Norway, 2021.
[63] A. Ogienagbon, M. Khalifeh, Experimental evaluation of the effect of temperature on the mechanical properties of setting materials for well integrity, SPE J. (2022) 1–13.
[64] N. Yong-Sing, L. Yun-Ming, H. Cheng-Yong, M.M.A.B. Abdullah, P. Pakawanit, L. W.L. Chan, N. Hui-Teng, O. Shee-Ween, O. Wan-En, H. Yong-Jie, Thin fly ash/ladle furnace slag geopolymer: effect of elevated temperature exposure on flexural properties and morphological characteristics, Ceram. Int. 48 (12) (2022) 16562–16575.
[65] Z. Abdollahnejad, A. Dalvand, M. Mastali, T. Luukkonen, M. Illikainen, Effects of waste ground glass and lime on the crystallinity and strength of geopolymers, Mag. Concr. Res. 71 (23) (2019) 1218–1231.
[66] A. Fernández-Jiménez, A. Palomo, 6 - nanostructure/microstructure of fly ash geopolymers, in: J.L. Provis, J.S.J. van Deventer (Eds.), Geopolymers, Woodhead Publishing2009, pp. 89-117..
[67] K. Somna, C. Jaturapitakkul, P. Kajitvichyanukul, P. Chindaprasirt, NaOH-activated ground fly ash geopolymer cured at ambient temperature, Fuel 90 (6) (2011) 2118–2124.
[68] S. Mani, B. Pradhan, Investigation on effect of fly ash content on strength and microstructure of geopolymer concrete in chloride-rich environment, Mater. Today: Proc. 32 (2020) 865–870.
[69] S. Kumar, G. Mucsi, F. Kristály, P. Pekker, Mechanical activation of fly ash and its influence on micro and nano-structural behaviour of resulting geopolymers, Adv. Powder Technol. 28 (3) (2017) 805–813.
[70] F.K. Lutgens, E.J. Tarbuck, D. Tasa, Essentials of Geology, Pearson, New York, 2014.
[71] S. Marshak, Essentials of Geology, WW Norton, 2004.
[72] M. Vafaei, A. Allahverdi, High strength geopolymer binder based on waste-glass powder, Adv. Powder Technol. 28 (1) (2017) 215–222.
[73] S. Yaseri, G. Hajiaghaei, F. Mohammadi, M. Mahdikhani, R. Farokhzad, The role of synthesis parameters on the workability, setting and strength properties of binary binder based geopolymer paste, Construct. Build. Mater. 157 (2017) 534–545.
[74] X. Xue, Y.-L. Liu, J.-G. Dai, C.-S. Poon, W.-D. Zhang, P. Zhang, Inhibiting efflorescence formation on fly ash–based geopolymer via silane surface modification, Cement Concr. Compos. 94 (2018) 43–52.
[75] F. Pacheco-Torgal, J. Labrincha, C. Leonelli, A. Palomo, P. Chindaprasit, Handbook of Alkali-Activated Cements, Mortars and Concretes, Elsevier, 2014.
[76] E.F. Vansant, P. Van Der Voort, K.C. Vrancken, Characterization and Chemical Modification of the Silica Surface, Elsevier, 1995.
[77] C. Finocchiaro, G. Barone, P. Mazzoleni, C. Leonelli, A. Gharzouni, S. Rossignol, FT-IR study of early stages of alkali activated materials based on pyroclastic deposits (Mt. Etna, Sicily, Italy) using two different alkaline solutions, Construct. Build. Mater. 262 (2020) 120095.
[78] G. Fang, M. Zhang, Multiscale micromechanical analysis of alkali-activated fly ash-slag paste, Cement Concr. Res. 135 (2020) 106141.
[79] J. Zhang, Y. He, Y.-p. Wang, J. Mao, X.-m. Cui, Synthesis of a self-supporting faujasite zeolite membrane using geopolymer gel for separation of alcohol/water mixture, Mater. Lett. 116 (2014) 167–170.
[80] J.R. Gasca-Tirado, A. Manzano-Ramírez, E.M. RiveraMuñoz, R. Velázquez-Castillo, M. Apátiga-Castro, R. Nava, A. Rodríguez-López, Ion Exchange in Geopolymers, New Trends in Ion Exchange Studies, 2018.
[81] D. Zhao, Y. Gao, S. Nie, Z. Liu, F. Wang, P. Liu, S. Hu, Self-assembly of honeycomb-like calcium-aluminum-silicate-hydrate (CASH) on ceramsite sand and its application in photocatalysis, Chem. Eng. J. 344 (2018) 583–593.
[82] S. Chatterji, Chemistry of alkali–silica reaction and testing of aggregates, Cement Concr. Compos. 27 (7–8) (2005) 788–795.
[83] S. Chatterji, A. Jensen, N. Thaulow, P. Christensen, Studies of alkali-silica reaction. Part 3. Mechanisms by which NaCl and Ca (OH) 2 affect the reaction, Cement Concr. Res. 16 (2) (1986) 246–254.
[84] G. Kovalchuk, P. Krienko, Producing Fire-And Heat-Resistant Geopolymers, Geopolymers, Elsevier, 2009, pp. 227–266.
[85] P. Krivenko, V. Kyrychok, Genesis of structure and properties of the zeolite-like cement matrices of the system Na (K)-Al 2 O 3-SiO 2-H 2 O within a temperature range of 20–1200° C, Advan. Geopolymer-Zeolite Compos. Synthes. Charact. (2021). IntechOpen.
[86] H.E. Bergna, W.O. Roberts, Colloidal Silica: Fundamentals and Applications, CRC Press, 2005.
[87] E. Papirer, Adsorption on Silica Surfaces, CRC Press, 2000.
[88] R. Sibbick, C. Page, Mechanisms affecting the development of alkali-silica reaction in hardened concretes exposed to saline environments, Mag. Concr. Res. 50 (2) (1998) 147–159.
[89] F.K. Crundwell, On the mechanism of the dissolution of quartz and silica in aqueous solutions, ACS Omega 2 (3) (2017) 1116–1127.
[90] Z. Ren, L. Wang, Y. Li, J. Zha, G. Tian, F. Wang, H. Zhang, J. Liang, Synthesis of zeolites by in-situ conversion of geopolymers and their performance of heavy metal ion removal in wastewater:A review, J. Clean. Prod. 349 (2022) 131441.
[91] Z.h. Liu, Q. Tang, C.m. Li, Y. He, X.m. Cui, Preparation of NaA zeolite spheres from geopolymer gels using a one-step method in silicone oil, Int. J. Appl. Ceram. Technol. 14 (5) (2017) 982–986.
[92] N. Norberg, G. Neusser, R. Wirth, D. Harlov, Microstructural evolution during experimental albitization of K-rich alkali feldspar, Contrib. Mineral. Petrol. 162 (3) (2011) 531–546.
[93] G. Yuan, Y. Cao, H.-M. Schulz, F. Hao, J. Gluyas, K. Liu, T. Yang, Y. Wang, K. Xi, F. Li, A review of feldspar alteration and its geological significance in sedimentary basins: from shallow aquifers to deep hydrocarbon reservoirs, Earth Sci. Rev. 191 (2019) 114–140.
[94] R.B. Saldanha, H.C. Scheuermann Filho, J.L.D. Ribeiro, N.C. Consoli, Modelling the influence of density, curing time, amounts of lime and sodium chloride on the durability of compacted geopolymers monolithic walls, Construct. Build. Mater. 136 (2017) 65–72.
[95] L. Tian, S. Dai, X. Yao, H. Zhu, Q. Wu, Z. Liu, S. Cheng, Effect of nucleation seeding and triisopropanolamine on the compressive strength, chloride binding capacity and microstructure of cement paste, J. Build. Eng. 52 (2022) 104382.
[96] D. Hou, T. Li, P. Wang, Molecular dynamics study on the structure and dynamics of NaCl solution transport in the nanometer channel of CASH gel, ACS Sustain. Chem. Eng. 6 (7) (2018) 9498–9509.
[97] C.N. Mohamed, P. Ranjith, J. Sanjayan, Mechanical properties of geopolymer cement in brine: its suitability as well cement for geological sequestration of carbon dioxide (CO2). ISRM International Symposium-Asian Rock Mechanics Symposium, ISRM, 2012. ISRM-ARMS7-2012-110.
[98] A. Duguid, M. Radonjic, G.W. Scherer, Degradation of cement at the reservoir/cement interface from exposure to carbonated brine, Int. J. Greenh. Gas Control 5 (6) (2011) 1413–1428.
[99] Y. Pan, C. Wu, X. Huang, Long-term durability testing on the MgO-activated slag cured in brine, Construct. Build. Mater. 144 (2017) 271–278.
[100] S. Ridha, A.I. Abd Hamid, C.K.A.H. Che Ku Mazuan, Influence of different brine water salinity on mechanical properties of fly ash-based geopolymer cement, Int. J. Struct. Integrity 9 (2) (2018) 142–152.
[101] H. Abdoulghafour, L. Luquot, P. Gouze, Characterization of the mechanisms controlling the permeability changes of fractured cements flowed through by CO2-rich brine, Environ. Sci. Technol. 47 (18) (2013) 10332–10338.
[102] J. Gonzalez-Estrella, J. Ellison, J.C. Stormont, N. Shaikh, E.J. Peterson, P. Lichtner, J.M. Cerrato, Saline brine reaction with fractured wellbore cement and changes in hardness and hydraulic properties, Environ. Eng. Sci. 38 (3) (2021) 143–153.
[103] W. Yan, H.-G. Wei, N.D. Muchiri, F.-L. Li, J.-R. Zhang, Z.-X. Xu, Degradation of chemical and mechanical properties of cements with different formulations in

CO2-containing HTHP downhole environment, Petrol. Sci. 20 (2) (2023) 1119–1128.
[104] M.H. Samarakoon, P.G. Ranjith, W.A.M. Wanniarachchi, Properties of well cement following carbonated brine exposure under HTHP conditions: a comparative study of alkali-activated and class G cements, Cement Concr. Compos. 126 (2022) 104342.
[105] M.H. Ozyurtkan, M. Radonjic, An experimental study of the effect of CO2 rich brine on artificially fractured well-cement, Cement Concr. Compos. 45 (2014) 201–208.
[106] C. Kang, T. Kim, Influence of brine on hydration reaction of calcium sulfoaluminate and slag blended cement, Case Stud. Constr. Mater. 18 (2023) e02159.
[107] W. Lee, J. Van Deventer, The interface between natural siliceous aggregates and geopolymers, Cement Concr. Res. 34 (2) (2004) 195–206.
[108] Z. Zhang, X. Yao, H. Wang, Potential application of geopolymers as protection coatings for marine concrete III. Field experiment, Appl. Clay Sci. 67 (2012) 57–60.
[109] C. Tennakoon, A. Shayan, J.G. Sanjayan, A. Xu, Chloride ingress and steel corrosion in geopolymer concrete based on long term tests, Mater. Des. 116 (2017) 287–299.
[110] P. Chindaprasirt, W. Chalee, Effect of sodium hydroxide concentration on chloride penetration and steel corrosion of fly ash-based geopolymer concrete under marine site, Construct. Build. Mater. 63 (2014) 303–310.
[111] O. Keleştemur, B. Demirel, Effect of metakaolin on the corrosion resistance of structural lightweight concrete, Construct. Build. Mater. 81 (2015) 172–178.
[112] N. Ganesan, R. Abraham, S.D. Raj, Durability characteristics of steel fibre reinforced geopolymer concrete, Construct. Build. Mater. 93 (2015) 471–476.
[113] M. Vafaei, A. Allahverdi, P. Dong, N. Bassim, Acid attack on geopolymer cement mortar based on waste-glass powder and calcium aluminate cement at mild concentration, Construct. Build. Mater. 193 (2018) 363–372.
[114] U. Javed, F.U.A. Shaikh, P.K. Sarker, Corrosive effect of HCl and H2SO4 exposure on the strength and microstructure of lithium slag geopolymer mortars, Construct. Build. Mater. 411 (2024) 134588.
[115] O.A. Mayhoub, A. Mohsen, Y.R. Alharbi, A.A. Abadel, A. Habib, M. Kohail, Effect of curing regimes on chloride binding capacity of geopolymer, Ain Shams Eng. J. 12 (4) (2021) 3659–3668.
[116] K. Pasupathy, J. Sanjayan, P. Rajeev, D.W. Law, The effect of chloride ingress in reinforced geopolymer concrete exposed in the marine environment, J. Build. Eng. 39 (2021) 102281.
[117] W. He, B. Li, X. Meng, Q. Shen, Compound effects of sodium chloride and gypsum on the compressive strength and sulfate resistance of slag-based geopolymer concrete, Buildings 13 (3) (2023) 675.
[118] S. Nastiti, J. Ekaputri, Effect of chloride ions on concrete with geopolymer coatings in coastal area. IOP Conference Series: Earth and Environmental Science, IOP Publishing, 2020 012043.
[119] P. He, Q. Wang, S. Fu, M. Wang, S. Zhao, X. Liu, Y. Jiang, D. Jia, Y. Zhou, Hydrothermal transformation of geopolymers to bulk zeolite structures for efficient hazardous elements adsorption, Sci. Total Environ. 767 (2021) 144973.
[120] H. Yan, C. Xue-min, L.-p. Liu, X.-d. Liu, J.-y. Chen, The hydrothermal transformation of solid geopolymers into zeolites, Microporous Mesoporous Mater. 161 (2012) 187–192.
[121] Y. Yang, J. Zhang, Y. Fu, D. Hou, B. Dong, Alkaline hydrothermal activation of molybdenum tailings to prepare one-part geopolymer: activation mechanism and strength, J. Mater. Res. Technol. (2023).
[122] H.R. Khalid, N. Lee, S.M. Park, N. Abbas, H.-K. Lee, Synthesis of geopolymer-supported zeolites via robust one-step method and their adsorption potential, J. Hazard Mater. 353 (2018) 522–533.
[123] N. Murayama, H. Yamamoto, J. Shibata, Mechanism of zeolite synthesis from coal fly ash by alkali hydrothermal reaction, Int. J. Miner. Process. 64 (1) (2002) 1–17.